Modelling and Piecewise-Affine Control of an Aerobatic Helicopter

Wei Yue

A Thesis

in

The Department

of

Mechanical and Industrial Engineering

Presented in Partial Fulfillment of the Requirements

for the Degree of Master of Applied Science (Mechanical Engineering) at

Concordia University

Montreal, Quebec, Canada

September 2005

Your file Votre référence
ISBN: 0-494-10277-2
Our file Notre référence
ISBN: 0-494-10277-2

Abstract

Modelling and Piecewise-Affine Control of an Aerobatic Helicopter

Wei Yue

The study of highly maneuverable aerobatic helicopters has received a growing amount of interest in the past few years. This thesis describes the development of an analytic dynamic model of an aerobatic helicopter with the least amount of complexity and with sufficient accuracy for control system development. The model is based on a rigid body dynamics formulation with applied external forces and moments including the effects of gravity and aerodynamics. The model is validated by comparing simulation results with flight test data available in the literature for a YAMAHA R-50 helicopter. The model is further simplified to obtain a three degree of freedom helicopter model and a piecewise-affine (PWA) approximate representation. The model is then used to develop a PWA controller for the system. To design this controller a local linear controller is designed for the PWA approximate model in the region where the desired closed-loop equilibrium point lies. An optimization problem subject to Bilinear Matrix Inequalities (BMIs) is then solved to find a PWA extension of the linear controller. A piecewise quadratic Lyapunov function is found which proves stability of the closed-loop system in the whole domain of the nonlinearity.

This work develops a physics-based model for aerobatic helicopters representing a complete derivation that allows approximations to be made to yield a simplified representation for PWA control design and analysis. The model is also expressed in a linear parameterized form ideal for parameter estimation and adaptive control. Finally, this research represents the first development of a PWA model and controller for an aerobatic helicopter system.

To my family

Table of Contents

List of Figures

Nomenclature

a	main rotor blade lift curve slope $(1/rad)$
a_t	tail rotor blade lift curve slope $(1/rad)$
c	rotor blade chord (m)
g	gravity acceleration (m/s^2)
h_m	main rotor hub height above c.g. (m)
h_t	tail rotor hub height above c.g. (m)
l_h	stabilizer location behind c.g. (m)
l_m	main rotor hub location behind c.g. (m)
l_t	tail rotor hub location behind c.g. (m)
m	helicopter mass (kg)
n_t	gear ratio of tail rotor to main rotor
p, q, r	angular velocity components of helicopter about fuselage x-,y-,z-axes (rad/s)
t	time (s)
u, v, w	translational velocity components of helicopter along fuselage x-,y-,z-axes (m/s)
x, y, z	mutually orthogonal directions of fuselage axes - x forward, y to starboard, z down; centered at the helicopter's center of mass (m)

C_{d0}	main rotor profile drag coefficient
C_{d0t}	tail rotor profile drag coefficient
C_h	horizontal stabilizer lift curve slope $(1/rad)$
C_{Tmax}	main rotor max thrust coefficient
C_{Ttmax}	tail rotor max thrust coefficient
C_v	vertical fin lift curve slope $(1/rad)$
I_β	flap moment of inertia (kgm^2)
I_{xx}, I_{yy}, I_{zz}	moments of inertia of the helicopter about the x-, y- and z-axes (kgm^2)
I_{xz}	product of inertia of the helicopter about the x- and z-axes (kgm^2)
K_β	hub torsional stiffness (Nm/rad)
K_μ	scaling of flap response to speed variation
L, M, N	external aerodynamic moments about the x-, y- and z-axes (Nm)
R	main rotor radius (m)
R_t	main rotor radius (m)
S_β	stiffness number
S_h	horizontal stabilizer area (m^2)
S_v	vertical fin area (m^2)
S_{xf}	frontal fuselage drag area (m^2)
S_{yf}	side fuselage drag area (m^2)
S_{zf}	vertical fuselage drag area (m^2)
T_m	main rotor thrust (N)
T_t	tail rotor thrust (N)

X, Y, Z	external aerodynamic forces applied along the x-, y- and z-axes (N)
X_f, Y_f, Z_f	components of X, Y, Z from fuselage(N)
X_h, Y_h, Z_h	components of X, Y, Z from horizontal stabilizer(N)
X_m, Y_m, Z_m	components of X, Y, Z from main rotor(N)
X_t, Y_t, Z_t	components of X, Y, Z from tail rotor(N)
X_v, Y_v, Z_v	components of X, Y, Z from vertical fin(N)
λ_0	main rotor uniform inflow velocity (normalized by ΩR)
λ_{0t}	tail rotor uniform inflow velocity (normalized by $\Omega_t R_t$)
λ_β	flap frequency ratio
μ	advance ratio (normalized by ΩR)
μ_t	nondimensional velocity at tail rotor (normalized by $\Omega_t R_t$)
θ_0, θ_{0t}	main and tail rotor collective pitch angles (rad)
ρ	air density (kg/m^3)
σ	main rotor solidity ratio
τ_β	time constant of rotor flap motion (s)
ϕ, θ, ψ	Euler angles defining the orientation of the aircraft relative to the Earth (rad)
Ψ	main rotor blade azimuth angle, positive in direction of rotor rotation (rad)
Ω	main rotor speed (rad/s)
Ω_t	tail rotor speed (rad/s)

Chapter 1

Introduction

1.1 Motivation

The study of aerobatic (miniature) helicopters has received a growing amount of interest in the past few years. Since they are more agile than full-scale helicopters, aerobatic helicopters can execute maneuvers that outperform most of the full-scale vehicles. Such miniature, highly agile air vehicles are suited to fly through confined spaces or in some challenging environments [23][6]. The modelling of aerobatic helicopters differs from that of full-scale helicopters in the following ways [6]:

- The rotor heads in aerobatic helicopters are relatively more rigid than those in full-scale helicopters, allowing for large rotor control moments. This is one of the main reasons why aerobatic helicopters are more agile than full-scale helicopters.

- Many aerobatic helicopters can produce negative thrust, allowing sustained inverted flight.

Given these important differences, the challenge of building a simple yet accurate aerobatic helicopter model for control design is one of the main motivations of this thesis. Furthermore, given that helicopters are highly nonlinear systems, the control

synthesis for complicated nonlinear systems is always a big challenge. One of the promising novel controller design methods appearing in the past few years was PWA controller synthesis. This methodology showed good performance applied to hybrid and switched systems [11][34]. The attempt to adopt PWA controller design synthesis to aerobatic helicopters is the other main challenge of this thesis.

1.2 Literature Review

There is an extensive body of literature on the dynamics of full-scale helicopters [2][32][46]. Procedures for building a simulation model were devised by Padfield [30]. One of the first comprehensive studies of aerobatic (miniature) helicopter models was performed by Mettler et. al. [26]. The authors developed and identified parameterized linear models for hover and forward flight conditions for the YAMAHA R-50 miniature helicopter using frequency domain methods. It was shown that miniature helicopters belonged to a different dynamic class from full-scale helicopters. Following the work by Mettler et. al., LaCivita et. al. [20] developed a technique that made use of the frequency response from multiple operating points, for the identification of key parameters of a more broadly descriptive nonlinear model. They applied the technique to a YAMAHA R-50 helicopter using the hover and cruise data collected in [23]. The obtained nonlinear model with 30 states was linearized to enable a fit with the local frequency response. The reduced-order, linearized model was similar to the one proposed by Mettler et. al. [26]. One of the first analytical nonlinear model of miniature helicopters in the literature was described by Gavrilets et. al. [6]. The work provided the rationale for the derivation of the equations of motion and documented the experimental methods used for the estimation of the model's parameters. The model was valid up to advance ratios (helicopter forward velocity/rotor blade tip speed) $\mu < 0.15$ for a variety of flight conditions, including negative rotor loading and

high angular rates. However, some of the helicopter dynamics in [6] were not well explained and the helicopter model needed further validation.

Nonlinear control of helicopters has also been studied in the literature (see Koo [16], Frazzoli [3] and references therein). T. J. Koo [16] illustrated the output tracking control design of a helicopter model based on approximate input-output linearization. By neglecting the coupling between forces and moments, it was shown that the approximate model with dynamic decoupling is full state linearizable by choosing positions and heading as output. It was proved that bounded tracking could be achieved by applying to the system the control input designed for the approximate model. E. Frazzoli [3] developed of a new computational and modelling framework (the Maneuver Automaton), and related algorithms, for a large class of autonomous vehicles including models of small autonomous helicopters. The proposed approach is based on a quantization of the systems dynamics, by which the feasible nominal system trajectories are restricted to the family of curves that can be obtained by the interconnection of suitably defined primitives. A fundamental advantage of this approach is the ability to provide a mathematical foundation for generating a provably stable and consistent hierarchical system, and for developing the tools to analyze the robustness of the system in the presence of uncertainty and/or disturbances. Shim et. al. [42] compared three different control methodologies for helicopter autopilot design: linear robust multi-variable control [10], fuzzy logic control with evolutionary tuning [47], and nonlinear tracking control. The simulation results showed that the robust and fuzzy controller were capable of handling uncertainties and disturbances.

However, the control methodologies in the literature have some limitations. The linear robust multi-variable control [10] and fuzzy logic control [47] quantify the uncertainties and unmodeled dynamics in the helicopter system. However they are conservative in the sense that the operating regime is limited to near hover conditions. Nonlinear tracking control covers a substantially wider range of flight envelopes, but

requires accurate knowledge about the helicopter system. Most of these works did not provide systematic output feedback controller design approaches with stability proof.

From the discussion in the previous paragraphs, we see that it is desirable to have a new controller design methodology for helicopters with stability guarantees and the possibility of systematic extension from state feedback to output feedback. In this thesis, PWA synthesis is applied to the nonlinear helicopter model. PWA systems became popular in the past few years. Johanson [11] performed a first comprehensive study of computational methods for analysis of piecewise-linear systems. Rodrigues [34][36] extended the analysis methodology to perform state and output feedback controller synthesis for PWA systems. Samadi and Rodrigues [40] developed a *MATLAB and SIMULINK*[1] toolbox for PWA controller synthesis for continuous-time nonlinear systems using the PENBMI [7] solver.

This thesis is the first successful attempt to apply PWA controller design methodologies to aerobatic helicopters. The advantages of this technique are [34][36][40]:

- *Possibility of using knowledge in linear controller design.* A linear controller can be designed to satisfy some performance index in a neighborhood of the desired closed-loop equilibrium point. Then, this linear controller is extended to the whole area of interest by adding affine pieces to it.

- *Effective global analysis tool.* Analysis of the obtained controller can be performed in a formal and numerically efficient way as a set of convex optimization problems. The solutions to these problems can determine bounds on performance, degree of stability and many other parameters of interest.

- *Proof of stability.* A Lyapunov function is found to prove stability of the closed-loop system.

[1]MATLAB and SIMULINK are trademarks of The Mathworks, Inc.

- *Systematic extension to output feedback controllers.* PWA control synthesis can be extended from state feedback controllers to output feedback controllers in a systematic way [34].

1.3 Thesis Outline and Contributions

The thesis contributions are:

- This work presents a physics-based model developed for aerobatic helicopters that allows approximations to be made to yield a simplified representation for PWA controller design and analysis. Furthermore, The model is then expressed in a linear parameterized form ideal for parameter estimation and adaptive control.

  A step-by-step process to develop a dynamic model for aerobatic helicopters is presented in chapter 2. In section 2.1, the equations of motion of a rigid body are derived. Then the external forces and moments existing in the equations of motion are analyzed and computed from section 2.2 to section 2.6. In section 2.2, the author takes great effort to explain the main rotor flapping dynamics, which is one of the most important factors in the modelling. The simulation and validation of the model are presented in section 2.8. Section 5.3 presents the method by which parameter estimation can be implemented.

- A three degree of freedom simplified nonlinear aerobatic helicopter model and its PWA approximation model are developed.

  In section 3.1, the six degree of freedom helicopter model developed in chapter 2 is simplified by restricting the motion of the helicopter to the lateral plane. In section 3.3, the PWA approximation is carried out.

- The first successful attempt to apply PWA control synthesis to a nonlinear helicopter model with two variables in the domain of the nonlinearity.

  In section 3.2, the control objective is stated and the dynamics of the model are presented. In section 3.4, a local linear controller for the region where the desired closed-loop equilibrium point lies is designed. Then, an optimization problem is solved to find a PWA controller that stabilizes the nonlinear system in the whole domain of interest and a piecewise quadratic Lyapunov function is found to prove stability of the closed-loop system.

Chapter 2

Helicopter Dynamics and Modelling

This chapter describes the six degree of freedom dynamic model of aerobatic helicopters. This model will be simplified to a three degree of freedom model and then a PWA controller for the three degree of freedom model will be developed in Chapter 3.

2.1 Equations of Motion

Deriving the equations of motion of the helicopter is the first step of the modelling process. It will be assumed that the helicopter is a rigid body. In this section the equations of motion of a rigid body are derived. The notation used is listed in table 2.1.

Table 2.1: Notations

u, v, w	translational velocity components of helicopter along fuselage x_B-,y_B-,z_B-axes
p, q, r	angular velocity components of helicopter along fuselage x_B-,y_B-,z_B-axes
X, Y, Z	external force components of helicopter along fuselage x_B-,y_B-,z_B-axes
L, M, N	external moment components of helicopter along fuselage x_B-,y_B-,z_B-axes
m	mass of the helicopter
$\vec{V}$	translational velocity vector
$\vec{\omega}$	angular velocity vector
$\vec{F}$	external force vector
$\vec{M}$	external moment vector
$\vec{H}$	angular momentum

2.1.1 Reference Frames

For deriving the equations of motion of the helicopter, it is convenient to define the body frame indicated in figure 2.1[1]. The origin lies in the center of gravity. The x_B-axis is fixed to a longitudinal reference line in the helicopter; the y_B-axis is oriented to the right and the z_B-axis downward.

Another reference frame that is very useful in formulating the equations of motion is the inertial (or Earth) frame. The origin lies in the center of gravity. The x_I-axis is horizontal pointing in the helicopter forward flight direction and the z_I-axis vertically downward. The y_I-axis is perpendicular to both. The angles between the body axes and the inertial axes are the roll angle ϕ, the pitch angle θ and the yaw angle ψ (see figure 2.1). These angles describe the orientation of the helicopter. The next section will focus on modelling the orientation.

[1]Figure 2.1, 2.3, 2.4, 2.5, 2.6, 2.23, 2.24 and 2.26 are modified from the Robinson R22 Beta helicopter picture [32].

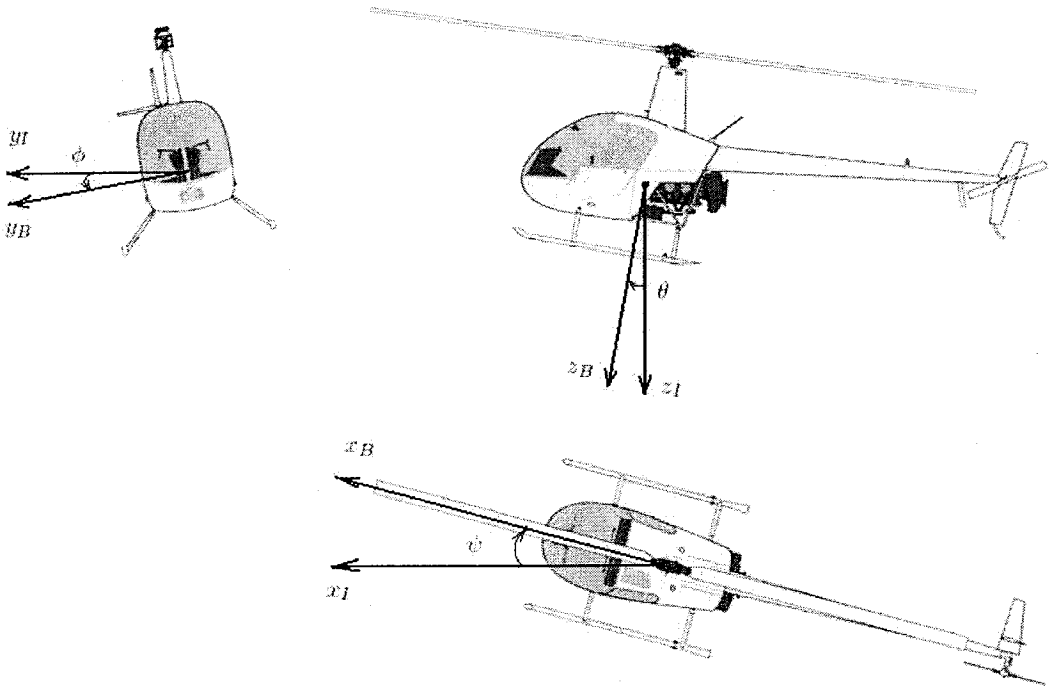

Figure 2.1: The body axes and the inertial axes of the helicopter

2.1.2 Euler Angles

A commonly used method to represent the orientation of vehicles in space is Euler angles. Euler angles make it possible to represent arbitrary orientations of a frame (e.g. the body frame) relative to another frame (e.g. the inertial frame) using the following transformations (see figure 2.2):

1. Align the origins of both systems.

2. Yaw about the unit vector $\mathbf{k_I}$ by an angle ψ. The unit vectors in the rotated frame can be related to those in the original inertial frame by the transformation

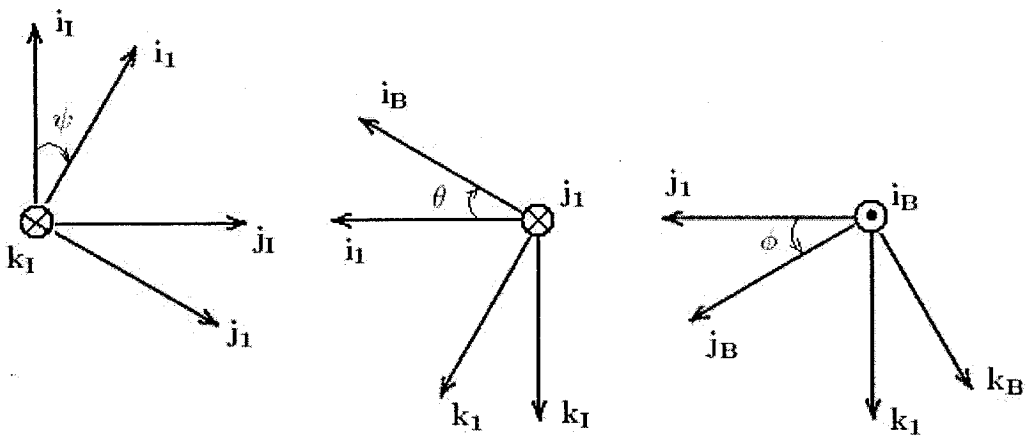

Figure 2.2: Euler angles

$\mathbf{\Psi}$, i.e.

$$\begin{bmatrix} \mathbf{i_1} \\ \mathbf{j_1} \\ \mathbf{k_I} \end{bmatrix} = \begin{bmatrix} \cos\psi & \sin\psi & 0 \\ -\sin\psi & \cos\psi & 0 \\ 0 & 0 & 1 \end{bmatrix} \begin{bmatrix} \mathbf{i_I} \\ \mathbf{j_I} \\ \mathbf{k_I} \end{bmatrix} \text{ or } \{\mathbf{b}\} = \mathbf{\Psi}\{\mathbf{a}\} \tag{2.1}$$

3. Pitch about the unit vector $\mathbf{j_1}$ by an angle θ, i.e.

$$\begin{bmatrix} \mathbf{i_B} \\ \mathbf{j_1} \\ \mathbf{k_1} \end{bmatrix} = \begin{bmatrix} \cos\theta & 0 & -\sin\theta \\ 0 & 1 & 0 \\ \sin\theta & 0 & \cos\theta \end{bmatrix} \begin{bmatrix} \mathbf{i_1} \\ \mathbf{j_1} \\ \mathbf{k_I} \end{bmatrix} \text{ or } \{\mathbf{c}\} = \mathbf{\Theta}\{\mathbf{b}\} \tag{2.2}$$

4. Roll about the unit vector $\mathbf{i_B}$ by an angle ϕ, i.e.

$$\begin{bmatrix} \mathbf{i_B} \\ \mathbf{j_B} \\ \mathbf{k_B} \end{bmatrix} = \begin{bmatrix} 1 & 0 & 0 \\ 0 & \cos\phi & \sin\phi \\ 0 & -\sin\phi & \cos\phi \end{bmatrix} \begin{bmatrix} \mathbf{i_B} \\ \mathbf{j_1} \\ \mathbf{k_1} \end{bmatrix} \text{ or } \{\mathbf{d}\} = \mathbf{\Phi}\{\mathbf{c}\} \tag{2.3}$$

Of particular interest is the relationship between the time rate of change of the orientation angles (ϕ, θ and ψ) and the fuselage angular velocities in the body axes system (p, q and r). From equations (2.1) - (2.3), the following relation can be derived.

$$\dot{\phi} = p + q\sin\phi\tan\theta + r\cos\phi\tan\theta \tag{2.4}$$

$$\dot{\theta} = q\cos\phi - r\sin\phi \tag{2.5}$$

$$\dot{\psi} = q\sin\phi\sec\theta + r\cos\phi\sec\theta \tag{2.6}$$

2.1.3 Equations of Motion

Although the equations of motion can be derived for any axes system, the body axes system is most convenient, especially for the moment equations because the moments of inertia remain constant.

The equations of motion are now derived step by step from the Newton equations of motion. The Newton equations of motion can be written in the vector forms as (see figure 2.3)

$$\overrightarrow{F} = \frac{d(m\overrightarrow{V})}{dt} \tag{2.7}$$

$$\overrightarrow{M} = \frac{d\overrightarrow{H}}{dt} \tag{2.8}$$

Then the forces and moments equations can be derived from equations (2.7) and (2.8), respectively as follows.

- Forces equations

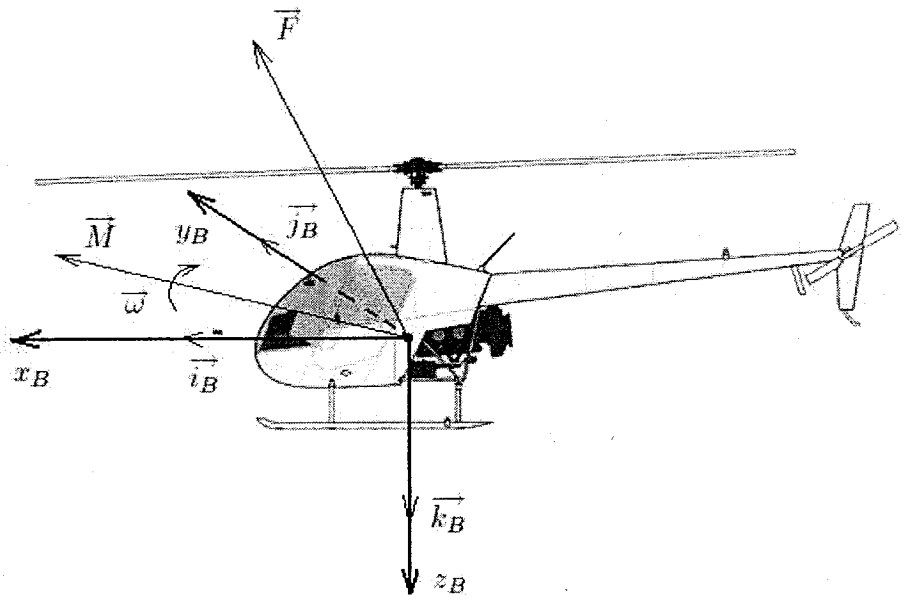

Figure 2.3: Forces and moments equations diagram

The force equation (2.7) can be resolved in body axes as

$$\begin{aligned}\overrightarrow{F} &= X\overrightarrow{i_B} + Y\overrightarrow{j_B} + Z\overrightarrow{k_B} \\ &= m\frac{d}{dt}(u\overrightarrow{i_B} + v\overrightarrow{j_B} + w\overrightarrow{k_B}) \\ &= m[(\dot{u}\overrightarrow{i_B} + u\frac{di_B}{dt}) + \cdots + (\dot{w}\overrightarrow{k_B} + w\frac{dk_B}{dt})]\end{aligned} \tag{2.9}$$

Since the body axes rotate at $\overrightarrow{\omega}$, we can write

$$d\frac{\overrightarrow{i_B}}{dt} = \overrightarrow{\omega} \times \overrightarrow{i_B} = r\overrightarrow{j_B} - q\overrightarrow{k_B} \tag{2.10}$$

$$d\frac{\overrightarrow{j_B}}{dt} = \overrightarrow{\omega} \times \overrightarrow{j_B} = -r\overrightarrow{i_B} + p\overrightarrow{k_B} \tag{2.11}$$

$$d\frac{\overrightarrow{k_B}}{dt} = \overrightarrow{\omega} \times \overrightarrow{k_B} = q\overrightarrow{i_B} - p\overrightarrow{j_B} \tag{2.12}$$

Substituting equations (2.10) - (2.12) into equation (2.9) yields

$$X = m(\dot{u} - rv + qw) \tag{2.13}$$

$$Y = m(\dot{v} + ru - pw) \tag{2.14}$$

$$Z = m(\dot{w} - ru + pv) \tag{2.15}$$

Rearranging equations (2.13) - (2.15) yields

$$\dot{u} = -wq + vr + \frac{X}{m} \tag{2.16}$$

$$\dot{v} = -ur + wp + \frac{Y}{m} \tag{2.17}$$

$$\dot{w} = -vp + uq + \frac{Z}{m} \tag{2.18}$$

- Moments equations

The moment equation (2.8) can be resolved in body axes as

$$\begin{aligned} \overrightarrow{M} &= L\overrightarrow{i_B} + M\overrightarrow{j_B} + N\overrightarrow{k_B} \\ &= \frac{d}{dt}(H_x\overrightarrow{i_B} + H_y\overrightarrow{j_B} + H_z\overrightarrow{k_B}) \end{aligned} \tag{2.19}$$

Similar to the method used in deriving the forces equations, the angular momentum can also be resolved in body axes as

$$H_x = I_{xx}p - I_{xy}q - I_{xz}r \tag{2.20}$$

$$H_y = -I_{xy}p + I_{yy}q - I_{yz}r \tag{2.21}$$

$$H_z = -I_{xz}p - I_{yz}q + I_{zz}r \tag{2.22}$$

where the moments of inertia are $I_{xx} = \sum \Delta m(y^2 + z^2)$, $I_{yy} = \sum \Delta m(x^2 + z^2)$ and $I_{zz} = \sum \Delta m(x^2 + y^2)$; the products of inertia are $I_{xy} = -\sum \Delta mxy$, $I_{xz} =$

$-\sum \Delta mxz$ and $I_{yz} = -\sum \Delta myz$. Considering that helicopters are commonly assumed to be symmetrical about the $x_B z_B$ plane, the following products of inertia are equal to zero (see figure 2.4).

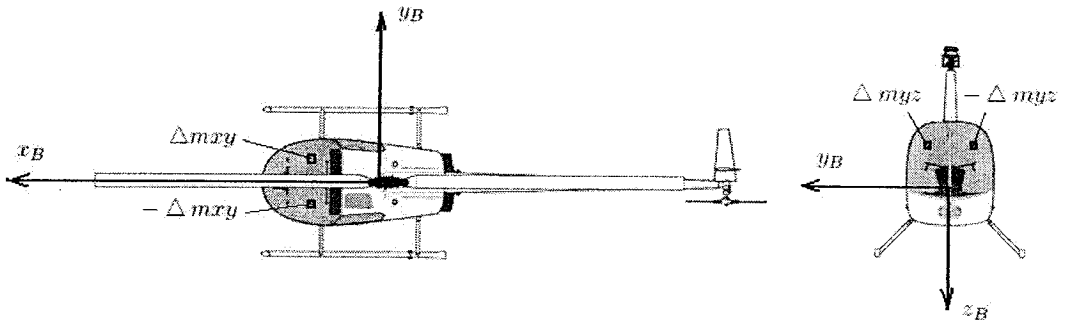

Figure 2.4: The symmetry of the helicopter

$$I_{xy} = -\sum \Delta mxy = 0$$
$$I_{yz} = -\sum \Delta myz = 0$$

Therefore, equations (2.20) - (2.22) transform to

$$H_x = I_{xx}\omega_x - I_{xz}\omega_z \tag{2.23}$$
$$H_y = I_{yy}\omega_y \tag{2.24}$$
$$H_z = -I_{xz}\omega_x + I_{zz}\omega_z \tag{2.25}$$

Substituting the angular momentum equations (2.23) - (2.25) and equations (2.10) - (2.12) into the moment equation (2.19) yields

$$M_x = I_{xx}\dot{p} + (I_{xx} - I_{yy})rq - I_{xz}(pq + \dot{r}) \tag{2.26}$$
$$M_y = I_{yy}\dot{q} + (I_{xx} - I_{zz})pr - I_{xz}(r^2 - p^2) \tag{2.27}$$
$$M_z = I_{zz}\dot{r} + (I_{yy} - I_{xx})pq - I_{xz}(\dot{p} - rq) \tag{2.28}$$

Rearranging, this yields

$$\dot{p} = \frac{(I_{yy} - I_{zz})}{I_{xx}} qr + \frac{I_{xz}}{I_{xx}}(pq + \dot{r}) + \frac{L}{I_{xx}} \tag{2.29}$$

$$\dot{q} = \frac{(I_{zz} - I_{xx})}{I_{yy}} rp + \frac{I_{xz}}{I_{yy}}(r^2 - p^2) + \frac{M}{I_{yy}} \tag{2.30}$$

$$\dot{r} = \frac{(I_{xx} - I_{yy})}{I_{zz}} pq + \frac{I_{xz}}{I_{zz}}(\dot{p} - rq) + \frac{N}{I_{zz}} \tag{2.31}$$

Finally, by grouping the forces equations (2.16) - (2.18), the moments equations (2.29) - (2.31) and Euler angles equations (2.4) - (2.6), the equations of motion of the helicopter are obtained and expressed as follows

$$\begin{aligned}
\dot{u} &= -wq + vr + \frac{X}{m} \\
\dot{v} &= -ur + wp + \frac{Y}{m} \\
\dot{w} &= -vp + uq + \frac{Z}{m} \\
\dot{p} &= \frac{(I_{yy} - I_{zz})}{I_{xx}} qr + \frac{I_{xz}}{I_{xx}}(pq + \dot{r}) + \frac{L}{I_{xx}} \\
\dot{q} &= \frac{(I_{zz} - I_{xx})}{I_{yy}} rp + \frac{I_{xz}}{I_{yy}}(r^2 - p^2) + \frac{M}{I_{yy}} \\
\dot{r} &= \frac{(I_{xx} - I_{yy})}{I_{zz}} pq + \frac{I_{xz}}{I_{zz}}(\dot{p} - rq) + \frac{N}{I_{zz}} \\
\dot{\phi} &= p + q \sin\phi \tan\theta + r \cos\phi \tan\theta \\
\dot{\theta} &= q \cos\phi - r \sin\phi \\
\dot{\psi} &= q \sin\phi \sec\theta + r \cos\phi \sec\theta
\end{aligned} \tag{2.32}$$

Solving the equations of motion (2.32) for the state variables u, v, w, p, q, r, ϕ, θ and ψ is the next and most important step of the modelling process. To do this, the forces and moments in the equations of motion (X, Y, Z, L, M and N) have to be computed and presented as functions of known parameters, state variables and pilot control inputs[2]. These forces and moments are shown along with the main

[2]Pilot control inputs include the main rotor collective control, the main rotor cyclic control and

helicopter variables in figure 2.5. To compute them, a component derivation method

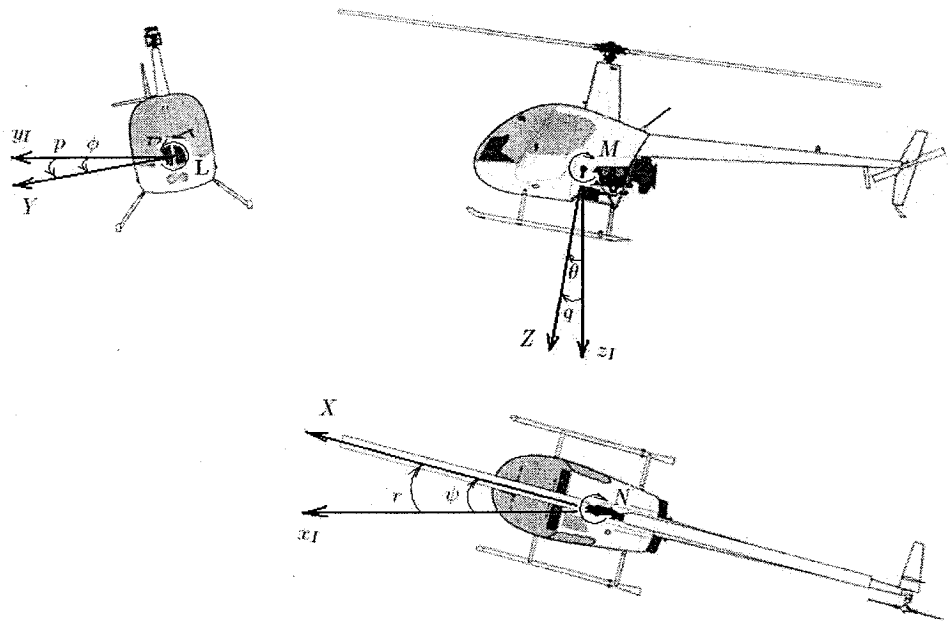

Figure 2.5: Forces and moments applied on a helicopter

is used. As shown in figure 2.6, a helicopter can be viewed as a complex arrangement of five interacting sub-systems which are the main rotor, the tail rotor, the horizontal stabilizer, the vertical fin and the fuselage. Therefore, the forces and moments can be presented as

$$\begin{bmatrix} X \\ Y \\ Z \\ L \\ M \\ N \end{bmatrix} = \begin{bmatrix} X_m \\ Y_m \\ Z_m \\ L_m \\ M_m \\ N_m \end{bmatrix} + \begin{bmatrix} X_t \\ Y_t \\ Z_t \\ L_t \\ M_t \\ N_t \end{bmatrix} + \begin{bmatrix} X_h \\ Y_h \\ Z_h \\ L_h \\ M_h \\ N_h \end{bmatrix} + \begin{bmatrix} X_v \\ Y_v \\ Z_v \\ L_v \\ M_v \\ N_v \end{bmatrix} + \begin{bmatrix} X_f \\ Y_f \\ Z_f \\ L_f \\ M_f \\ N_f \end{bmatrix} \tag{2.33}$$

where $()_m$, $()_t$, $()_h$, $()_v$ and $()_f$ are used to indicate the forces or moments applied

the tail rotor pedal control. These control inputs will be described in section 2.2 and 2.3.

on the five sub-systems, respectively. In the following sections, dynamics of the five sub-systems are described and the forces and moments applied on them are then computed, respectively.

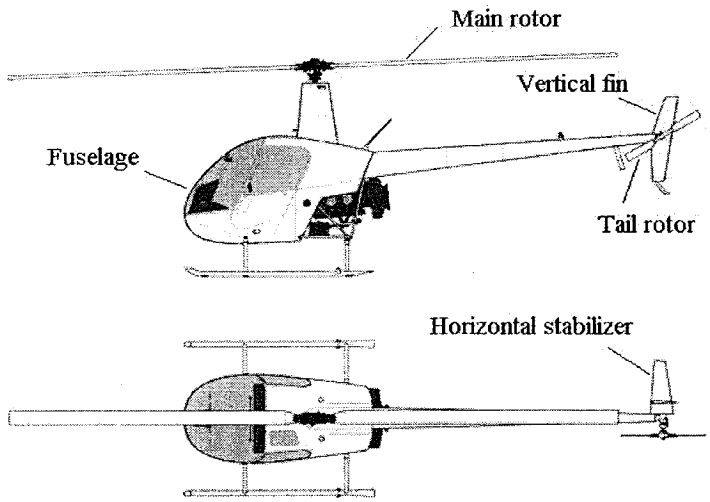

Figure 2.6: The helicopter as an arrangement of interacting sub-systems

2.2 Main Rotor

2.2.1 Terminology

It is necessary to introduce the terminology of the main rotor first as follows (see figure 2.7[3]).

- **Mast (shaft)** is the rotating shaft that connects the rotor blades to the helicopter.
- **Swash plate** turns non-rotating control movements into rotating control movements. The swash plate is made in two halves. The lower part is non-rotating

[3]Figure 2.7 is modified from the picture in http://www.delftoutlook.tudelft.nl/info/index80fb.html?hoofdstuk=Article&ArtID=5318.

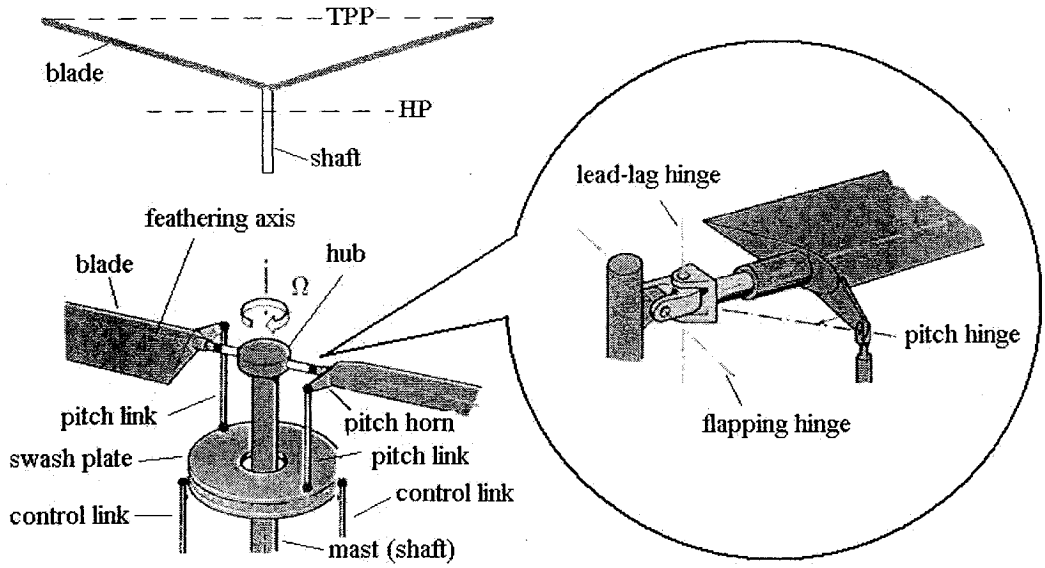

Figure 2.7: Terminology - the main rotor

and fitted with a spherical bearing so that the swash plate can tilt to any angle in any direction. The sphere can also slide up and down. The upper part is rotating with the rotor shaft.

- **Control links** are the push or pull tubes that change the pitch angle of the rotor blades.
- **Pitch links** connect the upper part of the swash plate and the pitch horns. They move up and down according to the swash plate such that the pitch angles of the blades are changed.
- **Pitch horn** is the armature that converts pitch link movement to blade pitch.
- **Hub** sits atop the mast and connects the rotor blades to the control links.
- **Feathering axis** is the spanwise axis about which a rotor blade rotates to change the pitch angle.
- **Flapping hinge** is the hinge that allows the blade to flap up and down freely.

- **Pitch hinge** is the hinge that allows the change of the blade pitch angle.
- **Lead-lag hinge** is the hinge that allows the blade to move back and forth (known as lead-lag motion) in the plane of the rotor.
- **Leading edge** is the forward facing edge of the rotor blade.
- **Trailing edge** is the back facing edge of the rotor blade.
- **Chord** is the distance from the leading edge to the trailing edge of the rotor blade.
- **Tip path plane (TPP)** is the plane whose boundary is described by the blade tips.
- **Rotor disk** is the disk whose boundary is described by the blade tips.
- **Hub plane (HP)** - The plane which is perpendicular to the rotor shaft.
- **Collective pitch control** moves the swash plate up or down to change pitch angles of all rotor blades in equal measure such that the rotor will produce more or less lift.
- **Cyclic pitch control** tilts the swash plate to change the pitch angle of each rotor blade periodically as it revolves such that the rotor disk can tilt in any direction.

With these mechanics the main rotor has three degree of freedom, i.e. rotation about the feathering axis which is known as blade pitch, bending up and down which is known as flapping and the lead-lag motion. Among these three motions, the only one that can be controlled actively by the pilot is the blade pitch. The flapping and the lead-lag motion are dominated by aerodynamic forces and blade pitch (figure 2.8).

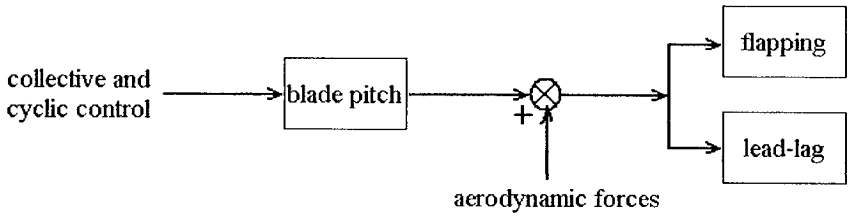

Figure 2.8: Degree of freedom of the main rotor

2.2.2 Flapping Dynamics

Since the flapping angle plays an important role in computing the forces and moments applied on the main rotor, dynamics and the mathematical model of the flapping angle are first described in this section.

Introduction

The up and down motion of the main rotor blades on their hinges is called the rotor flapping. As shown in figure 2.9, each of the blades is connected with the shaft by a flapping hinge, which allows the blade to bend up and down. The angle between each blade and the $x_B y_B$ plane is called the flapping angle β.

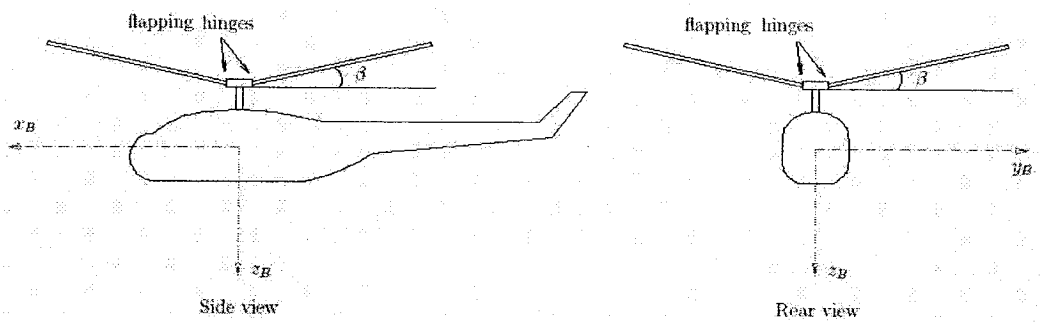

Figure 2.9: Definition of the rotor flapping

Before explaining the physical principle responsible for the rotor flapping it is necessary to review the expressions for the lift of an airfoil. Figure 2.10 shows the

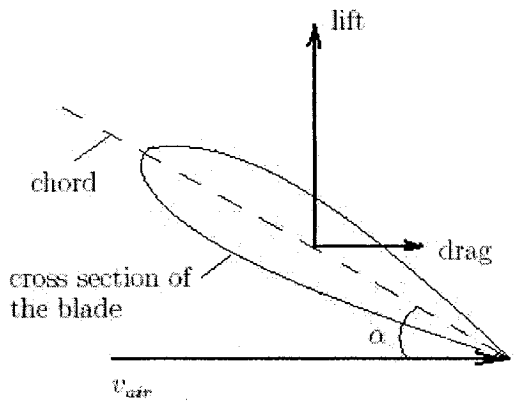

Figure 2.10: Lift generation of the rotor blade

cross section of a main rotor blade in the air. v_{air} is the air flow relative to the blade and α is the angle of attack. While the airstream is deflected downward by the airfoil, the lift and drag forces are created. From dimensional analysis, the lift is represented as $L = q_s C_L(\alpha) = \frac{1}{2}\rho v_{air}^2 S C_L(\alpha)$ [45], where q_s is the dynamic pressure ($q_s = \frac{1}{2}\rho v_{air}^2$), ρ is the air density, S is the surface area and $C_L(\alpha)$ is the lift coefficient that is a function of the angle of attack as shown in figure 2.11. The lift curve slope $a_0 = \frac{dC_L}{d\alpha}$

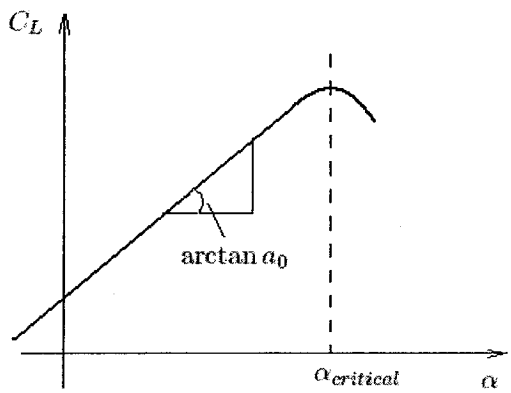

Figure 2.11: C_L vs. α

is fairly constant up to the stall angle $\alpha_{critical}$. Therefore, up to stall conditions, the lift of the rotor blade is proportional to the angle of attack and square of the air flow

velocity: $L \propto \alpha, v^2$.

The reason why the rotor flapping exists is because the dissymmetry of the lift on the rotor can be completely eliminated by the flapping motion. As shown in figure

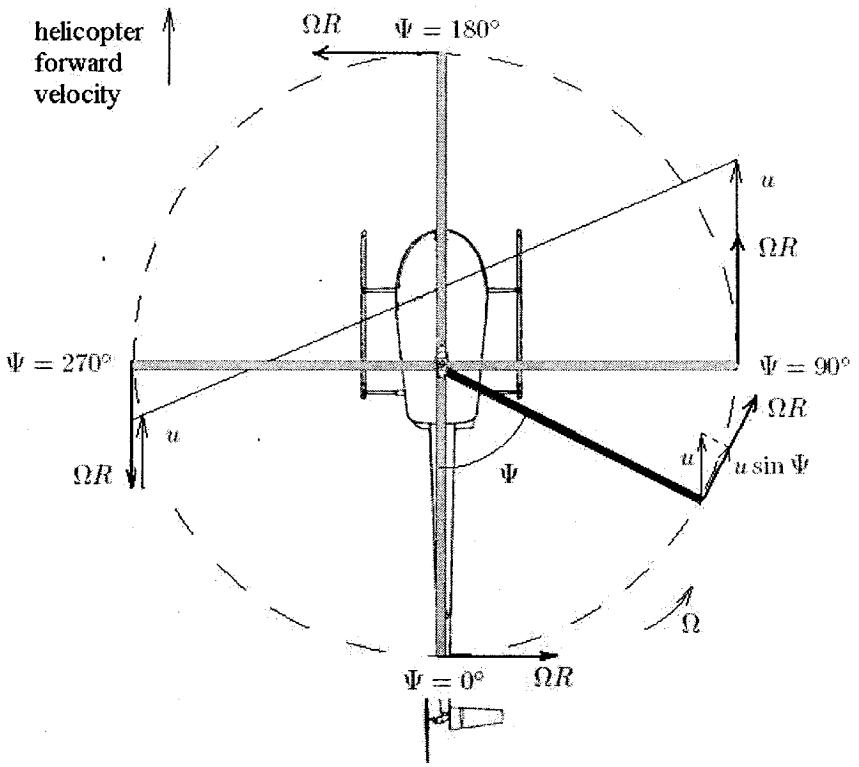

Figure 2.12: Blades velocities in forward flight

2.12, the helicopter is in forward flight condition with velocity u. The main rotor speed is assumed to be constant (Ω). R is the length of the blade and Ψ is the azimuth with $\Psi = 0°$ over the tail and positive counter-clockwise. The local velocity perpendicular to the leading edge of the blade tip is $v_{air} = \Omega R + u \sin \Psi$. Because of the sinusoidal variation on Ψ, over the tail and over the nose the blade tip sees the same velocity ($\sin \Psi = 0$), but on the advancing blade it sees a higher velocity ($\sin \Psi > 0$) while on the retreating blade a lower one ($\sin \Psi < 0$). If each blade had the same pitch setting, their angles of attack would be nearly the same, but the difference in velocity v_{air}

would produce more lift on the advancing blade than on the retreating blade. This would produce an unbalanced rolling moment, as shown in figure 2.13(a)[4], which would roll the helicopter over. However, the advancing blade, which initially has high

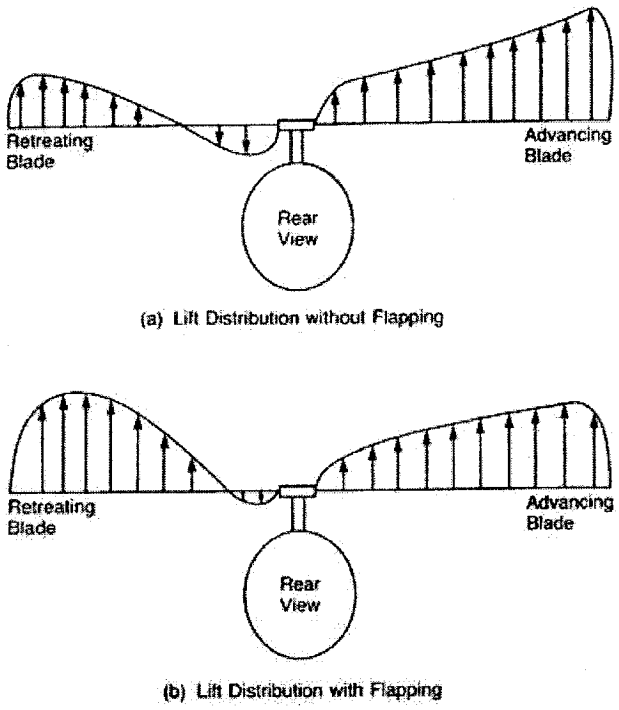

Figure 2.13: Effect of blade flapping on lateral lift distribution

lift, begins to accelerate upward. As it is accelerating upward, it is also being rotated toward the nose, where the local velocity v_{air} is reduced to its mean value (ΩR), such that no unbalanced lift exists and the blade stops accelerating. The retreating blade is undergoing a similar experience except that it is accelerating downward as it is rotated to a position over the tail. The flapping motion produces a climbing condition on the advancing blade. As a result, the angle of attack is decreased (see figure 2.14). The retreating blade, on the other hand, is descending and experiencing an increased angle of attack. The rotor comes to a flapping equilibrium when the local changes in angle of attack are just sufficient to compensate for the local changes

[4]Figure 2.13 is taken from the picture in [32].

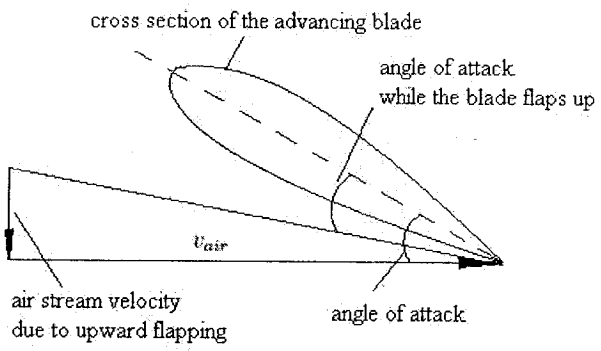

Figure 2.14: Change in angle of attack due to flapping

in dynamic pressure. Therefore, the unbalanced rolling moment is eliminated by the flapping motion (figure 2.13(b)).

The goal is to derive the dynamic equations of the rotor flapping. To do this, consider now the mathematical analysis of a rotating flapping blade in hover and in forward flight, respectively.

The Flapping in Hover

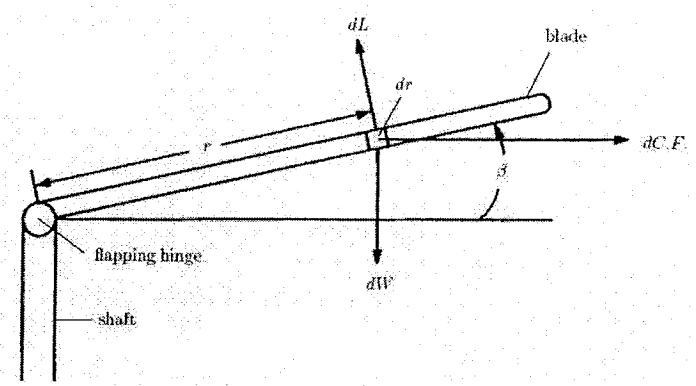

Figure 2.15: The rotor flapping in hover

Figure 2.15 shows a rigid rotor blade flapping in hover. The equilibrium position of the blade is determined by the balance of the aerodynamic force L, the centrifugal

force $C.F.$ and the weight of the blade W. Since the weight of the blade is very small with respect to the other two forces, it can be omitted in the mathematical analysis [21]. Given that the centrifugal forces are much larger than the aerodynamic forces, the flapping angle β is usually quite small (between 3-6 degrees is typical for a helicopter rotor [32]).

As before, it is assumed that the main rotor rotational speed about the shaft is constant (Ω). Assume an uniform mass per unit length of the blade, m. Considering a small element of the blade of length dr, the mass of this element is mdr (see figure 2.15). The contribution of this small element to the centrifugal force applied in a direction parallel to the plane of rotation is

$$d(C.F.) = (mdr)r\cos\beta\Omega^2 = m\Omega^2 r\cos\beta dr$$

Therefore, the total centrifugal force applied on the blade is

$$C.F. = \int_0^R m\Omega^2 r\cos\beta dr \approx \int_0^R m\Omega^2 r dr = \frac{m\Omega^2 R^2}{2} \tag{2.34}$$

The moment about the flapping hinge as a result of the centrifugal forces produced by all the elements is (the counter-clockwise direction in figure 2.15 is taken as positive for computing the moment)

$$\begin{aligned} M_{C.F.} &= -\int_0^R m\Omega^2 r\cos\beta r\sin\beta dr = -m\Omega^2\cos\beta\sin\beta\int_0^R r^2 dr \\ &= -\frac{m\Omega^2\cos\beta\sin\beta R^3}{3} \approx -\frac{m\Omega^2\beta R^3}{3} \end{aligned} \tag{2.35}$$

The aerodynamic moment about the flapping hinge is

$$M_L = \int_0^R r dL \tag{2.36}$$

The rotating blade will reach an equilibrium position where the centrifugal moment is equal and opposite to the aerodynamic moment (note that the gravity of the blade is ignored). Therefore the equilibrium equation can be written as

$$M_L + M_\beta = 0 \tag{2.37}$$

Thus the equilibrium flapping angle or coning angle β_0 is given by solving equations (2.35) - (2.37)

$$\beta_0 = \frac{\int_0^R r dL}{\frac{m\Omega^2 R^3}{3}} \tag{2.38}$$

It is constant and independent of azimuth Ψ in hover, while in forward flight it varies with respect to azimuth Ψ as shown in the following subsection.

The Flapping in Forward Flight

In forward flight, because of the variation of aerodynamic force with azimuth (refer to figure 2.12) the blade flaps up and down. Figure 2.16 shows the forces applied on the blade. The centrifugal moment about the hinge is (note that β is a small angle)

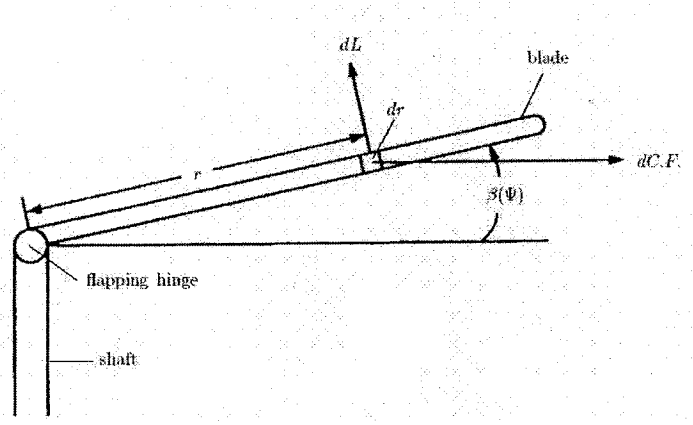

Figure 2.16: The rotor flapping in forward flight

$$dM_{C.F.} = -(mdr)r^2\Omega^2\beta = -mr^2\Omega^2\beta dr \tag{2.39}$$

The elementary inertial moment about the hinge is

$$-dI\ddot{\beta} = -(mdr)r^2\ddot{\beta} = -mr^2\ddot{\beta}dr \tag{2.40}$$

The aerodynamic moment about the hinge is

$$dM_L = rdL \tag{2.41}$$

Therefore, the equations of motion can be derived by summing the moments yielding

$$\int_0^R dM_{C.F.} - \int_0^R dI\ddot{\beta} + \int_0^R rdL = 0 \tag{2.42}$$

Substituting equations (2.39) - (2.41) into equation (2.42) yields

$$-\int_0^R mr^2\Omega^2\beta dr - \int_0^R mr^2\ddot{\beta}dr + \int_0^R rdL = 0 \tag{2.43}$$

The mass moment of inertia of the blade about the flapping hinge is

$$dI = mr^2dr \tag{2.44}$$

Rearranging equations (2.43) and (2.44) yields

$$I\ddot{\beta} + I\Omega^2\beta = \int_0^R rdL \tag{2.45}$$

The solution to equation (2.45) can be represented by an infinite Fourier series

$$\beta = a_0 - a_1\cos\Psi - b_1\sin\Psi - a_2\cos 2\Psi - b_2\sin 2\Psi - \cdots - a_n\cos n\Psi - b_n\sin n\Psi \tag{2.46}$$

Only the first three terms will be used because the second and higher harmonics are relatively small [32]. Therefore, it will be assumed that

$$\beta = a_0 - a_1 \cos \Psi - b_1 \sin \Psi \tag{2.47}$$

where a_0 represents the average value, which is the coning angle β_0 in equation (2.38), a_1 is called the longitudinal flapping angle defined as positive when the blade flaps down at the tail and up at the nose, and b_1 is the lateral flapping angle defined as positive when the blade flaps down on the advancing side and up on the retreating side. The physical description of a_1 and b_1 is discussed in the following subsections.

Physical Description of the Longitudinal Flapping

The coefficient a_1 represents the amplitude of the pure cosine flapping motion, which can also be regarded as a longitudinal or fore-aft tilt of the rotor tip path plane (TPP) (figure 2.17). In forward flight, the rotor disk has a tendency to tilt

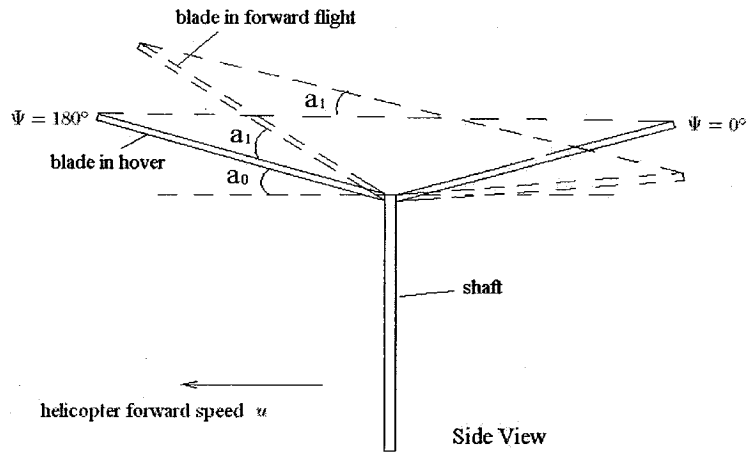

Figure 2.17: Longitudinal flapping

back (longitudinally) because of the dissymmetry in the lift produced between the advancing side of the disk (refer to section 2.2.2 - Introduction). As the blade rotates

into the advancing side of the disk, the excess lift causes the blade to flap upward. As the blade rotates into the retreating side of the rotor disk, the deficiency in lift causes the blade to flap downward. Therefore, over the front of the disk ($\Psi = 180°$) the blade reaches a maximum angular displacement with $\dot{\beta} = 0$. As a result of the upward or downward flapping, the blade lift, that would have increased on the advancing blade or decreased on the retreating blade if there was no flapping motion, is compensated due to the change of the local angle in attack (refer to section 2.2.2 - Introduction).

Physical Description of the Lateral Flapping

The coefficient b_1 represents the amplitude of the pure sine flapping motion, which can be regarded as a lateral or left-right tilt of the TPP (figure 2.18). This effect

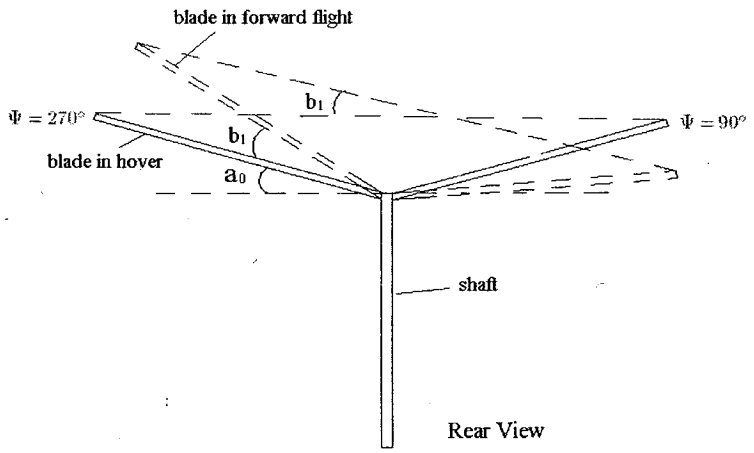

Figure 2.18: Lateral flapping

arises because of the blade flapping displacement (coning a_0). For the coning rotor in forward flight with velocity u, the blade over the nose ($90° < \Psi < 270°$) experiences an air component ($u \sin \beta$) coming toward its lower surface (see figure 2.19), while the blade over the tail ($270° < \Psi < 450°$) experiences air approaching it from the top. Therefore the local angle of attack is decreased when the blade is over the tail and increased when the blade is over the nose. The rotor compensates for this

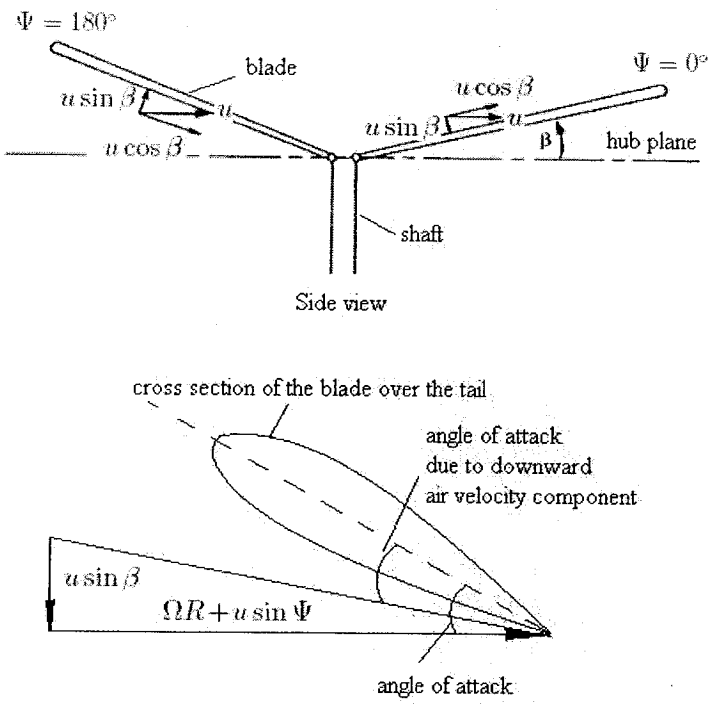

Figure 2.19: Change in angle of attack due to velocity orientation

inequality in the same manner as it did for the asymmetric velocity patterns on the advancing and retreating blades: the blade starts to flap upward when $\Psi = 90°$ and flap downward when $\Psi = 270°$. The result is that the difference in flapping velocities over the nose and over the tail compensates for the difference in the angle of attack caused by coning.

Dynamic Equations

Since the longitudinal flapping angle a_1 and the lateral flapping angle b_1 are necessary in computing the main rotor forces and moments, the dynamic equations of the rotor flapping are derived to solve for a_1 and b_1 in this subsetion. As shown in equation (2.45) the flapping dynamics can be represented by a second-order equation, from which the quasi-steady flapping equations can be derived. However, in this the-

sis first-order equations are used to describe the dynamics, which are more simple yet sufficiently accurate for our purpose [25][26][6]. The equations are expressed as

$$\dot{a_1} = -q - \frac{a_1}{\tau_e} + \frac{1}{\tau_e}\frac{\partial a_1}{\partial \mu_u}\mu_u + \frac{\delta_{lon}}{\tau_e} \tag{2.48}$$

$$\dot{b_1} = -p - \frac{b_1}{\tau_e} + \frac{1}{\tau_e}\frac{\partial b_1}{\partial \mu_v}\mu_v + \frac{\delta_{lat}}{\tau_e} \tag{2.49}$$

where $\mu_u = \frac{u}{\Omega R}$ and $\mu_v = \frac{v}{\Omega R}$ are the components of the nondimensional velocity of the helicopter, δ_{lon} and δ_{lat} are the longitudinal and lateral cyclic pilot control inputs and τ_e is the effective rotor time constant [6]. The derivatives $\frac{\partial a_1}{\partial \mu_u}$ and $\frac{\partial b_1}{\partial \mu_v}$ describe changes of the flapping angles due to the helicopter translational velocity components u and v. Theoretical values for the steady-state longitudinal flapping and lateral flapping for a rotor without a stabilizer bar are given in [2] as

$$\frac{\partial a_1}{\partial \mu_u} = -\frac{\partial b_1}{\partial \mu_v} = 2(\frac{4\delta_{col}}{3} - \lambda_0) \tag{2.50}$$

The stabilizer bar is widely used in aerobatic helicopters. It reduces flapping response to gusts. Equation (2.50) cannot be used for a rotor equipped with such a device. Since these derivatives ($\frac{\partial a_1}{\partial \mu_u}$ and $\frac{\partial b_1}{\partial \mu_v}$) play a primary role in the frequency and damping of the phugoid mode, which is very slow, it is difficult to estimate it using frequency domain identification methods [26]. An open loop excitation would have to last for much longer than it takes for the helicopter to diverge, therefore the necessary pilot's feedback would bias an estimate of the derivative [22]. In [6], a scaling coefficient is introduced in equation (2.50), yielding

$$\frac{\partial a_1}{\partial \mu_u} = -\frac{\partial b_1}{\partial \mu_v} = 2K_\mu(\frac{4\delta_{col}}{3} - \lambda_0) \tag{2.51}$$

The scaling coefficient K_μ tells us how much the stabilizer bar reduces the steady-state flapping response to the helicopter forward velocity u and side slip velocity v.

A rough estimate for K_μ can be obtained by matching the steady-state cyclic input in forward flight at constant speed (maintained with the velocity-tracking feedback controller) with that predicted by the simulation under the same conditions [6].

2.2.3 Main Rotor Forces and Moments

In this section the main rotor forces (X_m, Y_m and Z_m) and moments (L_m, M_m and N_m) in the equations of motion (2.32) are presented. Since they are functions of the rotor thrust T_m and torque Q_m, we will compute T_m and Q_m first.

Thrust

The main rotor thrust T_m is the aerodynamic force perpendicular to the TPP. It can be computed from the integration of the elementary lift dL on each blade element dr along the blade and around the azimuth (figure 2.20(a)). The lift for each blade

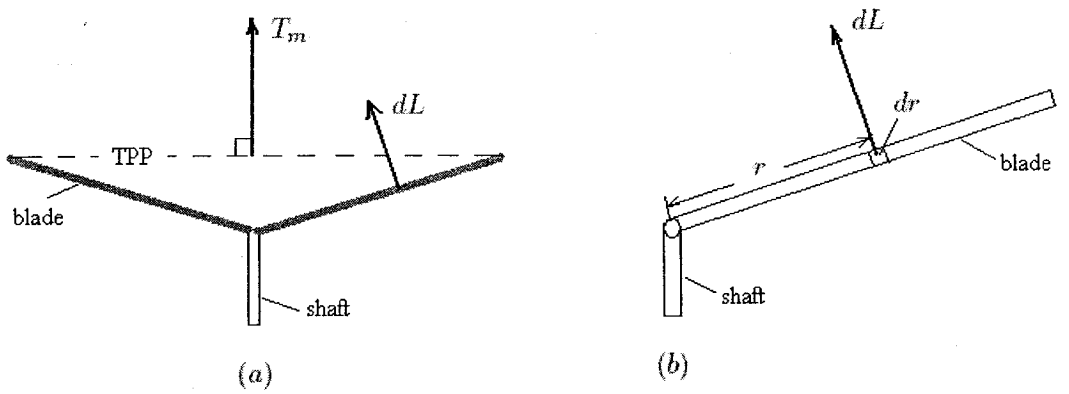

Figure 2.20: Main rotor thrust

element can be written as

$$dL = \frac{1}{2}\rho U_T^2 C_L c dr \tag{2.52}$$

where c is the span of the blade, U_T is the tangential component of the air velocity (v_{air}, refer to figure 2.10) relative to the blade and U_P is the perpendicular component

of the air velocity (see figure 2.21). C_L is the lift coefficient which can be written as

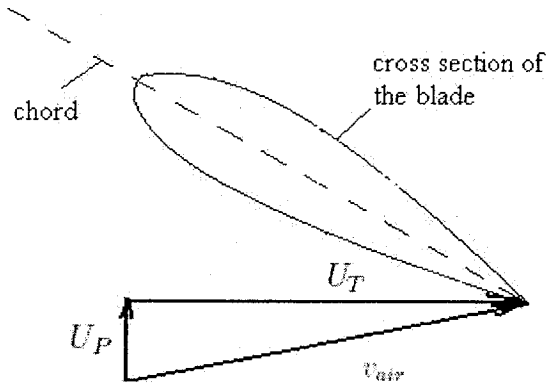

Figure 2.21: Main rotor thrust

(refer to figure 2.11)

$$C_L = a\alpha$$

where a is the lift curve slope of the main rotor. Therefore, equation (2.52) transforms to

$$dL = \frac{1}{2}\rho U_T^2 a\alpha c dr \tag{2.53}$$

The integration procedure is complicated. In this thesis only the main steps and results are presented. Details can be found in [30] and [32]. The lift per running foot is

$$\frac{dL}{dr} = \frac{1}{2}\rho U_T^2 a\alpha c \tag{2.54}$$

The average lift per blade around the azimuth can be written as

$$\overline{L} = \frac{1}{2\pi}\int_0^{2\pi}(\int_0^R \frac{dL}{dr}dr)d\Psi \tag{2.55}$$

The total thrust is equal to the number of blades (b) times the average lift per blade expressed as

$$T_m = \frac{b}{2\pi}\int_0^{2\pi}(\int_0^R \frac{dL}{dr}dr)d\Psi \tag{2.56}$$

Substituting equation (2.52) into equation (2.56) and rearranging in the nondimensional form[5] yields

$$C_T = \frac{a\sigma}{2}\int_0^{2\pi}(\int_0^1 (\frac{U_T}{\Omega R})^2\theta + \frac{U_P}{\Omega R}\frac{U_T}{\Omega R})d\frac{r}{R}d\Psi \tag{2.57}$$

where $\sigma = \frac{bc}{\pi R}$ is the solidity ratio and θ is the pitch angle of each blade. The integration of equation (2.57) results in

$$C_T = \frac{a\sigma}{2}(\theta_0(\frac{1}{3}+\frac{\mu^2}{2}) + \frac{\mu_z - \lambda_0}{2}) \tag{2.58}$$

where $\mu = \frac{\sqrt{u^2+v^2}}{\Omega R}$ is the advance ratio, $\mu_z = \frac{w}{\Omega R}$ is nondimensional form of the vertical velocity component, θ_0 is the rotor collective pitch angle which is proportional to the pilot collective pitch control input [30], and λ_0 is nondimensional form of the rotor inflow ($\lambda_0 = \frac{v_i}{\Omega R}$). The thrust T_m is written as

$$T_m = \rho(\Omega R)^2\pi R^2 C_T \tag{2.59}$$

From equation (2.58) and (2.59), it is shown that the thrust T_m is a function of θ_0, μ, μ_z and λ_0. Among them, the rotor inflow λ_0 is an unknown variable. Therefore, in order to compute the thrust, the rotor inflow should first be computed. The following subsection describes the process.

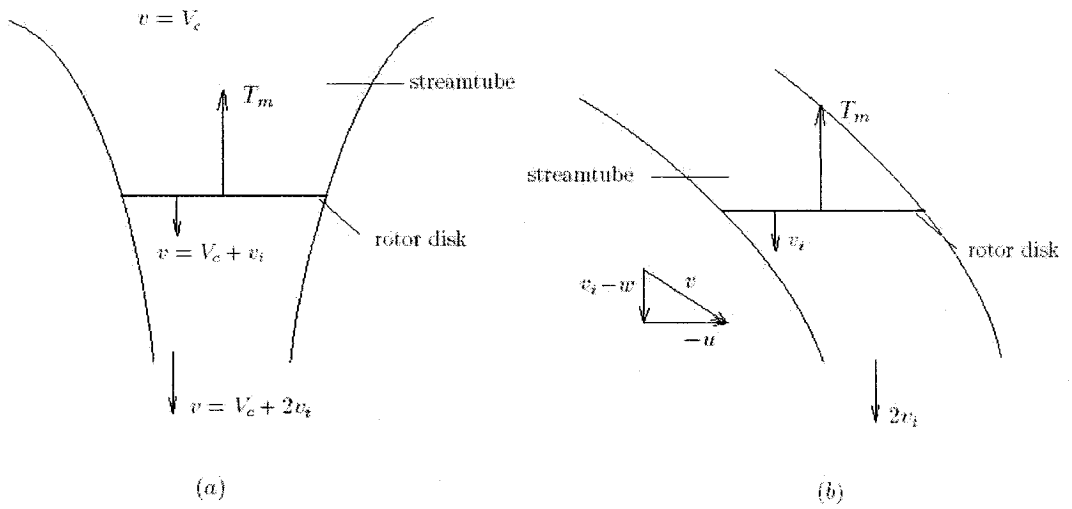

Figure 2.22: The rotor inflow in climb (a) and forward flight (b) motion

Rotor Inflow

The rotor inflow is the flow field induced by the rotor at the rotor disk, thus contributing to the local blade incidence and dynamic pressure [30]. Figure 2.22(a) shows the rotor inflow in hover condition. The velocity at various stations in the streamtube v is shown[6] and where v_i is the inflow velocity at the rotor disk.

Note that the relationship between C_T and λ_0 in equation (2.58) is obtained by integrating the elementary blade lift, momentum theory allows us to derive another relationship between them. First consider the climb condition (the helicopter is climbing with speed V_c). The mass flow through the rotor is written as

$$\dot{m} = \rho A_d (V_c + v_i) \tag{2.60}$$

where A_d is the rotor disk area. The rate of change of momentum between the

[5]Nondimensionalizing is done by dividing the thrust T_m by $\rho(\Omega R)^2 \pi R^2$ or dividing the torque Q_m by $\rho(\Omega R)^2 \pi R^3$. The resulting nondimensional form of T_m and Q_m are thrust coefficient C_T and torque coefficient C_Q, respectively.

[6]To avoid introducing more symbols, v is used here. Readers should note that it is different from the fuselage translational velocity component v.

undisturbed upstream conditions and the far wake can be equated to the rotor loading, yielding

$$T_m = \dot{m}(V_c + v_{i_\infty}) - \dot{m}V_c \tag{2.61}$$

where v_{i_∞} is the induced flow in the fully developed wake. The change in kinetic energy of the flow can be related to the work done by the rotor as

$$T_m v_i = \frac{1}{2}\dot{m}(V_c + v_i)^2 - \frac{1}{2}\dot{m}V_c^2 \tag{2.62}$$

From equations (2.61) and (2.62) it can be shown that the induced velocity in the far wake is twice the rotor inflow velocity, i.e.

$$v_{i_\infty} = 2v_i \tag{2.63}$$

The expression for the rotor thrust can then be written as

$$T_m = 2\rho A_d(V_c + v_i)v_i \tag{2.64}$$

Now consider the forward flight condition (see figure 2.22(b)). The induced flow in the far wake is again twice the flow at the rotor (see equation (2.63)). The mass flow through the rotor is

$$\dot{m} = \rho A_d v \tag{2.65}$$

where in forward flight $v = \sqrt{u^2 + (v_i - w)^2}$ (see figure 2.22(b)). The rotor thrust is then expressed as

$$T_m = \dot{m}2v_i = 2\rho A_d\sqrt{u^2 + (v_i - w)^2}v_i \tag{2.66}$$

Rearranging in the nondimensional form yields

$$\lambda_0 = \frac{C_T}{2\sqrt{\mu^2 + (\lambda_0 - \mu_z)^2}} \tag{2.67}$$

where $\lambda_0 = \frac{v_i}{\Omega R}$, $\mu = \frac{u}{\Omega R}$ and $\mu_z = \frac{w}{\Omega R}$.

Finally, given equations (2.58) and (2.67), C_T and λ_0 can be solved iteratively. The thrust T_m can then be derived by substituting C_T into equation (2.59). The magnitude of the main rotor thrust is limited based on the assumed maximum thrust T_{mmax} to model stall of the blades and other viscous losses.

Torque

The main rotor torque can be approximated as a sum of the induced torque due to the generated thrust and the torque due to the profile drag on the blades [30], yielding

$$C_Q = C_T(\lambda_0 - \mu_z) + \frac{C_{D0}\sigma}{8}(1 + \frac{7}{3}\mu^2) \tag{2.68}$$

where C_Q is the torque coefficient and C_{D0} is the profile drag coefficient of the main rotor blade. The yawing moment produced by the main rotor is then given by

$$Q_m = C_Q \rho (\Omega R)^2 \pi R^3 \tag{2.69}$$

Forces and Moments

Given that the thrust and torque are derived in the previous subsections, the equations of the main rotor forces and moments can be written by computing the components of the thrust and torque (see figure 2.23)

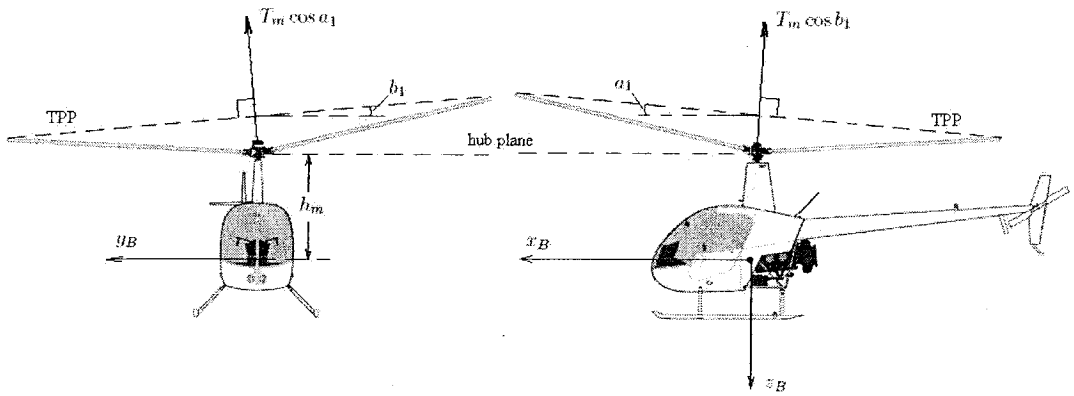

Figure 2.23: Main rotor forces and moments

$$X_m = -T_m \sin a_1 \tag{2.70}$$

$$Y_m = T_m \sin b_1 \tag{2.71}$$

$$Z_m = -T_m \cos a_1 \cos b_1 \tag{2.72}$$

$$L_m = K_\beta b_1 + T_m h_m \sin b_1 \tag{2.73}$$

$$M_m = K_\beta a_1 + T_m h_m \sin a_1 \tag{2.74}$$

$$N_m = Q_m \cos a_1 \cos b_1 \tag{2.75}$$

where h_m is the height of the main rotor hub with respect to the center of gravity. The terms $K_\beta b_1$ and $K_\beta a_1$ in equations (2.73) and (2.74) result from the restraint in the blade attachment to the rotor head. The restraint can be approximated using a linear torsional spring with a constant stiffness coefficient K_β resulting in a rolling moment $K_\beta b_1$ or a pitching moment $K_\beta a_1$. The second terms in equations (2.73) and (2.74) result from the tilting of the thrust vector. Assuming that the thrust vector is perpendicular to the TPP, the thrust vector will tilt proportionally to the rotor flapping angles resulting in a rolling moment $T_m h_m \sin b_1$ or a pitching moment $T_m h_m \sin a_1$.

Except for the hover condition, the rotor in-plane force, which contributes to the

drag and side force, is substantially smaller than the drag provided by the fuselage and the side force from the fuselage and the empennage. The rotor in-plane force is therefore neglected in the calculations. The moments due to the in-plane force are much smaller than those due to the blade flapping and therefore also neglected. Notice that the flapping angles a_1 and b_1 are small angles. Therefore, we have $\sin a_1 \approx a_1$, $\sin b_1 \approx b_1$, $\cos a_1 \approx 1$ and $\cos b_1 \approx 1$. The main rotor forces and moments equations (2.70) - (2.75) can then be simplified as

$$X_m = -T_m a_1 \tag{2.76}$$

$$Y_m = T_m b_1 \tag{2.77}$$

$$Z_m = -T_m \tag{2.78}$$

$$L_m = K_\beta b_1 + T_m h_m b_1 \tag{2.79}$$

$$M_m = K_\beta a_1 + T_m h_m a_1 \tag{2.80}$$

$$N_m = Q_m \tag{2.81}$$

2.2.4 Summary

As a summary, the algorithm for computing the main rotor forces and moments are as follows.

1. Solve equations (2.58) and (2.67) iteratively for the thrust coefficient C_T and the rotor inflow λ_0.

2. Substitute C_T into equation (2.59) to obtain the main rotor thrust T_m.

3. Substitute C_T into equation (2.68) and C_Q into equation (2.69) to obtain the main rotor torque Q_m.

4. Solve the dynamic equations of the rotor flapping (2.48) and (2.49) for the flapping angles a_1 and b_1.

5. Substitute T_m, Q_m, a_1 and b_1 into equations (2.76) - (2.81) to obtain the main rotor forces and moments X_m, Y_m, Z_m, L_m, M_m and N_m.

2.3 Tail Rotor

In this section, the forces and moments applied on the tail rotor are computed. The basic equations for the tail rotor forces and moments are similar to those for the main rotor. The analytical expressions for the tail rotor coefficients are approximated in this section. This can be done by adapting the methods used for computing the main rotor coefficients. First, we need to determine the normal (μ_{zt}) and the in-plane (μ_t) tail rotor inflow components. The main rotor wake effect plays an important role in the computation of (μ_{zt}) and (μ_t). This is discussed in the next subsection.

2.3.1 Main Rotor Wake Effect

The main rotor wake affects the tail rotor thrust in a complex way. To model this influence accurately an extensive modelling of the wake is required. However, a simple way used in this thesis is to approximate the increase in an apparent in-plane velocity seen by the tail rotor [6]. This velocity is defined as

$$w_{wake} = K_\lambda v_i \tag{2.82}$$

where v_i is the main rotor induced (inflow) velocity and K_λ is the main rotor wake intensity factor, which describes the extent the tail rotor is affected by the main rotor wake. The wake angle γ is defined as the angle between the main rotor induced velocity and the z_B axis in the $x_B z_B$ plane, i.e. $\gamma = \tan^{-1}\frac{u}{v_i - w}$. To compute K_λ, first compute the wake angles (figure 2.24) as

$$g_i = \tan\gamma_i = \frac{l_t - R - R_t}{h_m - h_t} \quad \text{and} \quad g_f = \tan\gamma_f = \frac{l_t - R}{h_m - h_t - R_t} \tag{2.83}$$

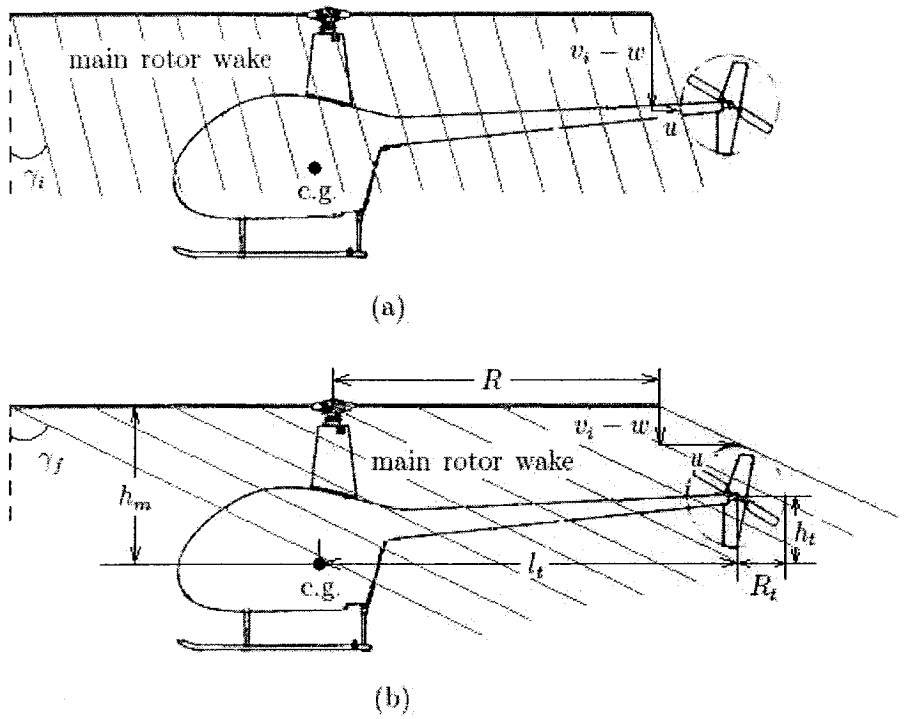

Figure 2.24: The main rotor wake effect

where l_t is the distance between the tail rotor and the center of gravity, R is the main rotor radius, R_t is the tail rotor radius, h_m is the main rotor hub height above the c.g. and h_t is the tail rotor hub height above the c.g. The tail rotor is out of the downwash if $v_i \leq w$, in which case there is an effective upwash. At low enough forward speed with respect to the air, the tail rotor is out of the wake as well (figure 2.24(a)). These two conditions can be represented by

$$tan^{-1}(\frac{u}{v_i - w}) \leq \gamma_i \quad \text{or} \quad \frac{u}{v_i - w} \leq g_i \tag{2.84}$$

In both of these cases $K_\lambda = 0$.

The tail rotor is fully in the wake (figure 2.24(b)) if

$$tan^{-1}(\frac{u}{v_i - w}) \geq \gamma_f \quad \text{or} \quad \frac{u}{v_i - w} \geq g_f \tag{2.85}$$

In the far wake, the downwash velocity is twice the value of that at the rotor (see equation (2.63)). It is assumed that $K_\lambda = 1.5$ when the tail rotor is fully immersed. In the remaining case, when the tail rotor is partially immersed, a linear growth of the wake intensity factor with the forward speed is assumed [6] as

$$K_\lambda = 1.5\frac{\frac{u}{v_i - w} - g_i}{g_f - g_i} \tag{2.86}$$

Next, we determine an advance ratio for the tail rotor

$$\mu_t = \frac{\sqrt{u^2 + w_t^2}}{\Omega_t R_t} \tag{2.87}$$

where $w_t = w + l_t q - K_\lambda v_i$ is the vertical velocity component of the tail rotor and Ω_t is the tail rotor speed. The velocity component normal to the tail rotor is given by

$$v_t = v - l_t r + h_t p \tag{2.88}$$

or in nondimensional form

$$\mu_{zt} = \frac{v_t}{\Omega_t R_t} \tag{2.89}$$

Given μ_t and μ_{zt}, similar to the computation of the main rotor thrust coefficient, the tail rotor thrust coefficient C_{Tt} and the tail rotor inflow λ_{0t} can be obtained by solving the following equations iteratively.

$$\lambda_{0t} = \mu_{zt} - 2[\frac{2C_{Tt}}{a_t \sigma_t} - \theta_{0t}(\frac{1}{3} + \frac{\mu_t^2}{2})] \tag{2.90}$$

$$C_{Tt} = 2\lambda_{0t}\sqrt{\mu_t^2 + (\mu_{zt} - \lambda_{0t})^2} \tag{2.91}$$

where a_t is the tail rotor blade lift curve slope, σ_t is the tail rotor solidity ratio and θ_{0t} is the tail rotor collective pitch angle which is proportional to the pilot pedal control

input [30]. The thrust T_t is then written as

$$T_t = \rho(\Omega_t R_t)^2 \pi R_t^2 C_{Tt} \tag{2.92}$$

The magnitude of the tail rotor thrust is limited based on the assumed maximum thrust T_{tmax} to model stall of the blades and other viscous losses. The torque of the tail rotor can be calculated the same way as the rotor torque was computed and is represented as

$$C_{Qt} = C_{Tt}(\mu_{zt} - \lambda_{0t}) + \frac{C_{D0t}\sigma}{8}(1 + 3\mu_t^2) \tag{2.93}$$

$$Q_t = C_{Qt}\rho(\Omega_t R_t)^2 \pi R_t^3 \tag{2.94}$$

where C_{D0t} is the tail rotor profile drag coefficient.

2.3.2 Tail Rotor Forces and Moments

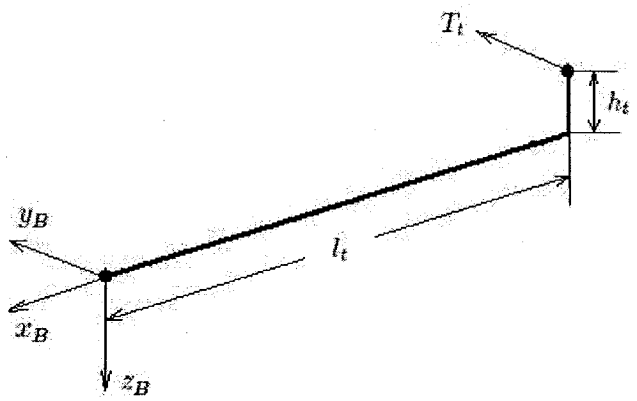

Figure 2.25: Tail rotor layout

Finally, the tail rotor forces and moments can be written (figure 2.25). The forces

are

$$X_t = 0 \tag{2.95}$$

$$Y_t = T_t \tag{2.96}$$

$$Z_t = 0 \tag{2.97}$$

The pitching moment generated by the tail rotor is equal to the tail rotor torque

$$M_t = Q_t \tag{2.98}$$

The yawing and rolling moments due to offsets from the c.g. are computed as follows (figure 2.26)

$$M_t = Q_t \tag{2.99}$$

$$N_t = -T_t l_t \tag{2.100}$$

$$L_t = T_t h_t \tag{2.101}$$

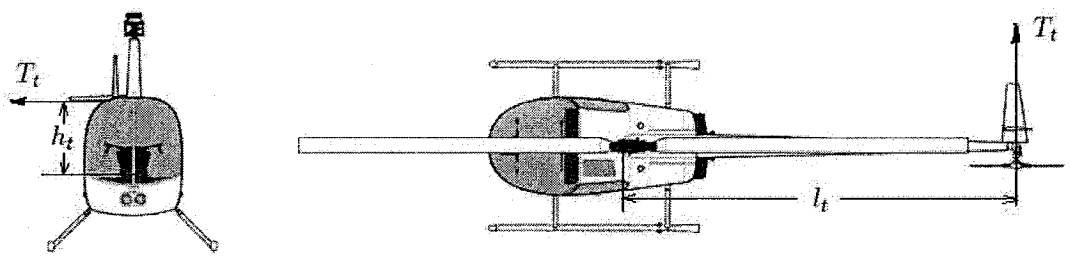

Figure 2.26: Moments of the tail rotor

2.3.3 Summary

As a summary, the algorithm for computing the tail rotor forces and moments are as follows.

1. Determine the normal (μ_{zt}) and the in-plane (μ_t) tail rotor inflow components from equations (2.87) and (2.89) and substitute these parameters into equations (2.90) and (2.91).

2. Solve equations (2.90) and (2.91) iteratively for the thrust coefficient C_{Tt} and the rotor inflow λ_{0t}.

3. Substitute C_{Tt} into equation (2.92) to obtain the tail rotor thrust T_t.

4. Substitute C_{Tt} into equations (2.93) and (2.94) to obtain the tail rotor torque Q_t.

5. Substitute T_t and Q_t into equations (2.95) - (2.101) to obtain the tail rotor forces and moments X_t, Y_t, Z_t, L_t, M_t and N_t.

2.4 Horizontal Stabilizer

In this section, the forces and moments applied on the horizontal stabilizer are computed. The horizontal stabilizer generates a Z-force that provides pitch damping and enhances pitch stability. Figure 2.27 shows the layout of the horizontal stabilizer. The Z-force Z_h consists of two components that are generated by the x_B-axis airflow and z_B-axis airflow, respectively.

- *Z-force component generated by the x_B-axis airflow (u).* As shown in figure 2.27, α_h is the horizontal stabilizer angle of attack. The force generated by the x_B-axis airflow can be presented in the same way the aerodynamic lift of an

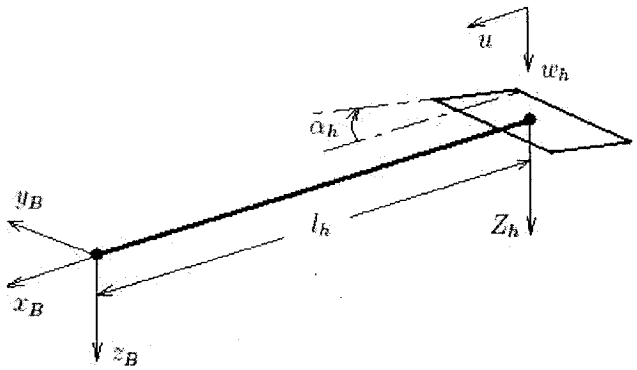

Figure 2.27: Horizontal stabilizer layout

airfoil is described:

$$Z_{h1} = -\frac{1}{2}\rho S_h C_h u^2 \tag{2.102}$$

where C_h is the horizontal stabilizer lift curve slope and S_h is the horizontal stabilizer area.

- *Z-force component generated by the z_B-axis airflow.* Assuming that the horizontal stabilizer may be fully or partially submerged in the wake of the main rotor (refer to section 2.3), an effective vertical velocity at the horizontal stabilizer location is determined by

$$w_h = w + l_h q - K_\lambda v_i \tag{2.103}$$

where w, $l_h q$ and $-K_\lambda v_i$ are the effective velocity components caused by the helicopter downward motion, the pitch motion and the main rotor wake, respectively.

The Z-force caused by w_h is then presented in the same way the aerodynamic drag of a flat plate is described:

$$Z_{h2} = -sign(w_h)\frac{1}{2}\rho S_h w_h^2 \tag{2.104}$$

Therefore, given equation (2.102) and (2.104), the total Z-force generated by the horizontal stabilizer is determined by

$$\begin{aligned} Z_h &= Z_{h1} + Z_{h2} \\ &= -\frac{1}{2}\rho S_h (C_h u^2 + |w_h| w_h) \end{aligned} \tag{2.105}$$

The Z-force creates a pitching moment due to the offsets from the c.g., yielding

$$M_h = Z_h l_h \tag{2.106}$$

The other forces and moments are equal to zero, i.e.

$$X_h = 0 \tag{2.107}$$

$$Y_h = 0 \tag{2.108}$$

$$L_h = 0 \tag{2.109}$$

$$N_h = 0 \tag{2.110}$$

2.5 Vertical Fin

In this section, the forces and moments applied on the vertical fin are computed. The vertical fin generates a side force that provides yaw damping and enhances yaw stability. Figure 2.28 shows the layout of the vertical fin. The side force Y_v consists of two components that are generated by the x_B-axis airflow and y_B-axis airflow, respectively.

- *Side force component generated by the x_B-axis airflow (u).* As shown in figure 2.28, β_v is the vertical fin angle of attack. The force generated by x_B-axis airflow

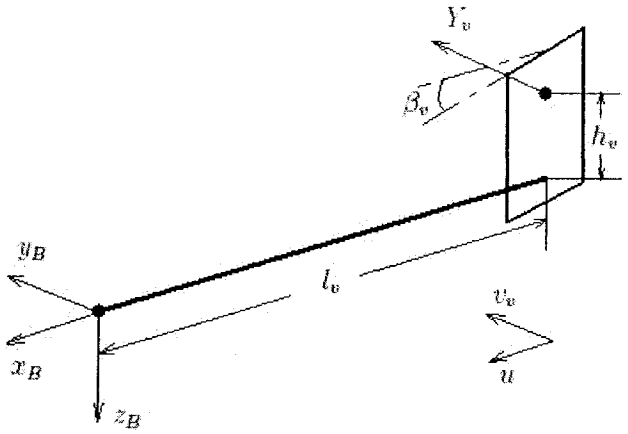

Figure 2.28: Vertical fin layout

can be presented in the same way the aerodynamic lift of an airfoil is described:

$$Y_{v1} = -\frac{1}{2}\rho S_v C_v u^2 \tag{2.111}$$

where C_v is the vertical fin lift curve slope and S_v is the vertical fin area.

- *Side force component generated by the y_B-axis airflow.* An effective Y-axis velocity at the vertical fin location is determined by

$$v_v = v - l_t r + \epsilon_v v_{it} \tag{2.112}$$

where v_{it} is the induced velocity from the tail rotor and ϵ_v is the fraction of the vertical fin area exposed to full induced velocity from the tail rotor. v, $-l_t r$ and $\epsilon_v v_{it}$ are the effective velocity components caused by the helicopter side slip motion, the yaw motion and the tail rotor inflow, respectively.

The side force caused by the y_B-axis airflow is then presented in the same way

the aerodynamic drag of a flat plate is described:

$$Y_{v2} = -sign(v_v)\frac{1}{2}\rho S_v v_v^2 \tag{2.113}$$

Therefore, given equation (2.111) and (2.113), the total side force generated by the vertical fin is determined by

$$\begin{aligned} Y_v &= Y_{v1} + Y_{v2} \\ &= -\frac{1}{2}\rho S_v (C_v u^2 + |v_v| v_v) \end{aligned} \tag{2.114}$$

The vertical fin side force creates a yawing moment and a rolling moment due to the offsets from the c.g., yielding

$$N_v = -Y_v l_t \tag{2.115}$$

$$L_v = Y_v h_t \tag{2.116}$$

The other forces and moments are equal to zero, i.e.

$$X_v = 0 \tag{2.117}$$

$$Z_v = 0 \tag{2.118}$$

$$N_v = 0 \tag{2.119}$$

2.6 Fuselage

In this section, the forces and moments applied on the fuselage are computed. For hovering or forward flight speeds well below the induced velocity at hover, the rotor downwash is deflected by the forward and side velocity components. This deflection creates a force opposing the movement. We express the X_f, Y_f and Z_f drag forces

created by the fuselage in this flight regime by [6]

$$X_f = -\frac{1}{2}\rho S_{xf} v_i^2 \frac{u}{v_i} \tag{2.120}$$

$$Y_f = -\frac{1}{2}\rho S_{yf} v_i^2 \frac{v}{v_i} \tag{2.121}$$

$$Z_f = -\frac{1}{2}\rho S_{zf} v_i^2 \frac{w}{v_i} \tag{2.122}$$

where S_{xf}, S_{yf} and S_{zf} are the effective drag areas of the fuselage in the X, Y and Z directions.

When the forward speed is higher than the rotor induced velocity, the fuselage drag can be modeled as the drag of a flat plate exposed to dynamic pressure [6]. In this case the perturbations to the fuselage forces can be expressed as

$$X_f = -\frac{1}{2}\rho S_{xf} U_e^2 \frac{u}{U_e} \tag{2.123}$$

$$Y_f = -\frac{1}{2}\rho S_{yf} U_e^2 \frac{v}{U_e} \tag{2.124}$$

$$Z_f = -\frac{1}{2}\rho S_{zf} U_e^2 \frac{w}{U_e} \tag{2.125}$$

where U_e is the trim airspeed.

Considering equations (2.120) - (2.125), the fuselage forces can be approximated to be

$$X_f = -\frac{1}{2}\rho S_{xf} u \sqrt{u^2 + v^2 + (w - v_i)^2} \tag{2.126}$$

$$Y_f = -\frac{1}{2}\rho S_{yf} v \sqrt{u^2 + v^2 + (w - v_i)^2} \tag{2.127}$$

$$Z_f = -\frac{1}{2}\rho S_{zf} (w - v_i) \sqrt{u^2 + v^2 + (w - v_i)^2} \tag{2.128}$$

It is assumed that the center of gravity and the center of aerodynamic force of the

fuselage coincide. Therefore, no fuselage moments are created, i.e.

$$L_f = 0 \tag{2.129}$$

$$M_f = 0 \tag{2.130}$$

$$N_f = 0 \tag{2.131}$$

2.7 Complete Model

All of the external forces and moments are presented in sections 2.2 - 2.6. Substituting these forces and moments into the equations of motion (2.32) yields the dynamic model of the helicopter. As a summary, all of the equations used in the modelling are included in this section.

- *Equations of motion.*

$$\begin{aligned}
\dot{u} &= -wq + vr + \frac{X}{m} - g\sin\theta \\
\dot{v} &= -ur + wp + \frac{Y}{m} + g\cos\theta\sin\phi \\
\dot{w} &= -vp + uq + \frac{Z}{m} + g\cos\theta\cos\phi \\
\dot{p} &= \frac{(I_{yy} - I_{zz})}{I_{xx}}qr + \frac{I_{xz}}{I_{xx}}(pq + \dot{r}) + \frac{L}{I_{xx}} \\
\dot{q} &= \frac{(I_{zz} - I_{xx})}{I_{yy}}rp + \frac{I_{xz}}{I_{yy}}(r^2 - p^2) + \frac{M}{I_{yy}} \\
\dot{r} &= \frac{(I_{xx} - I_{yy})}{I_{zz}}pq + \frac{I_{xz}}{I_{zz}}(\dot{p} - rq) + \frac{N}{I_{zz}} \\
\dot{\phi} &= p + q\sin\phi\tan\theta + r\cos\phi\tan\theta \\
\dot{\theta} &= q\cos\phi - r\sin\phi \\
\dot{\psi} &= q\sin\phi\sec\theta + r\cos\phi\sec\theta
\end{aligned} \tag{2.132}$$

where, $X = X_m + X_f$, $Y = Y_m + Y_f + Y_t + Y_v$, $Z = Z_m + Z_f + Z_h$,
$L = L_m + L_t + L_v$, $M = M_m + M_t + M_h$, $N = N_m + N_t + N_v$

- *Flapping dynamics.*

$$\dot{a_1} = -q - \frac{a_1}{\tau_e} + \frac{1}{\tau_e}\frac{\partial a_1}{\partial \mu_u}\mu_u + \frac{\delta_{lon}}{\tau_e} \tag{2.133}$$

$$\dot{b_1} = -p - \frac{b_1}{\tau_e} + \frac{1}{\tau_e}\frac{\partial b_1}{\partial \mu_v}\mu_v + \frac{\delta_{lat}}{\tau_e} \tag{2.134}$$

where,

$$\frac{\partial a_1}{\partial \mu} = -\frac{\partial b_1}{\partial \mu_v} = 2K_\mu(\frac{4\delta_{col}}{3} - \lambda_0) \tag{2.135}$$

- *Main rotor forces and moments.*

$$C_T = \frac{a\sigma}{2}(\theta_0(\frac{1}{3} + \frac{\mu^2}{2}) + \frac{\mu_z - \lambda_0}{2}) \tag{2.136}$$

$$\lambda_0 = \frac{C_T}{2\sqrt{\mu^2 + (\lambda_0 - \mu_z)^2}} \tag{2.137}$$

$$C_Q = C_T(\lambda_0 - \mu_z) + \frac{C_{D0}\sigma}{8}(1 + \frac{7}{3}\mu^2) \tag{2.138}$$

$$T_m = C_T\rho(\Omega R)^2\pi R^2 \tag{2.139}$$

$$Q_m = C_Q\rho(\Omega R)^2\pi R^3 \tag{2.140}$$

$$X_m = -T_m a_1 \tag{2.141}$$

$$Y_m = T_m b_1 \tag{2.142}$$

$$Z_m = -T_m \tag{2.143}$$

$$L_m = K_\beta b_1 + T_m h_m b_1 \tag{2.144}$$

$$M_m = K_\beta a_1 + T_m h_m a_1 \tag{2.145}$$

$$N_m = Q_m \tag{2.146}$$

- *Tail rotor forces and moments.*

$$g_i = \frac{l_t - R - R_t}{h_m - h_t} \tag{2.147}$$

$$g_f = \frac{l_t - R}{h_m - h_t - R_t} \tag{2.148}$$

$$K_\lambda = 1.5\frac{\frac{u}{v_i - w} - g_i}{g_f - g_i} \tag{2.149}$$

$$v_t = v - l_t r + h_t p \tag{2.150}$$

$$w_t = w + l_t q - K_\lambda v_i \tag{2.151}$$

$$\mu_t = \frac{\sqrt{u^2 + w_t^2}}{\Omega_t R_t} \tag{2.152}$$

$$\tag{2.153}$$

$$\mu_{zt} = \frac{v_t}{\Omega_t R_t} \tag{2.154}$$

$$\lambda_{0t} = \mu_{zt} - 2[\frac{2C_{Tt}}{a_t \sigma_t} - \theta_{0t}(\frac{1}{3} + \frac{\mu_t^2}{2})] \tag{2.155}$$

$$\lambda_{0t} = \frac{C_{Tt}}{2\sqrt{\mu_t^2 + (\mu_{zt} - \lambda_{0t})^2}} \tag{2.156}$$

$$C_{Qt} = C_{Tt}(\mu_{zt} - \lambda_{0t}) + \frac{C_{D0t}\sigma}{8}(1 + 3\mu_t^2) \tag{2.157}$$

$$T_t = C_{Tt}\rho(\Omega_t R_t)^2 \pi R_t^2 \tag{2.158}$$

$$Q_t = C_{Qt}\rho(\Omega_t R_t)^2 \pi R_t^3 \tag{2.159}$$

$$Y_t = T_t \tag{2.160}$$

$$L_t = T_t h_t \tag{2.161}$$

$$M_t = -Q_t \tag{2.162}$$

$$N_t = -T_t l_t \tag{2.163}$$

- *Horizontal stabilizer forces and moments.*

$$w_h = w + l_h q - K_\lambda v_i \tag{2.164}$$

$$Z_h = -\frac{1}{2}\rho S_h (C_h u^2 + |w_h| w_h) \tag{2.165}$$

$$M_h = Z_h l_h \tag{2.166}$$

- *Vertical fin forces and moments.*

$$v_{it} = \lambda_{0t} \Omega_t R_t \tag{2.167}$$

$$v_v = v - l_t r + \epsilon_v v_{it} \tag{2.168}$$

$$Y_v = -\frac{1}{2}\rho S_v (C_v u^2 + |v_v| v_v) \tag{2.169}$$

$$N_v = -Y_v l_t \tag{2.170}$$

$$L_v = Y_v h_t \tag{2.171}$$

- *Fuselage forces and moments*

$$X_f = -\frac{1}{2}\rho S_{xf} u \sqrt{u^2 + v^2 + (w - v_i)^2} \tag{2.172}$$

$$Y_f = -\frac{1}{2}\rho S_{yf} v \sqrt{u^2 + v^2 + (w - v_i)^2} \tag{2.173}$$

$$Z_f = -\frac{1}{2}\rho S_{zf} (w - v_i) \sqrt{u^2 + v^2 + (w - v_i)^2} \tag{2.174}$$

2.8 Model Validation

In this section, the developed model will be evaluated and validated by comparing the simulation results with flight test data available in the literature [26].

2.8.1 Simulation of the Model

The simulation of the model developed in this chapter is implemented in the *MATLAB and SIMULINK* environment. Figure 2.29 shows the simulation structure. The control inputs consist of the main rotor cyclic and lateral pitch controls, the main rotor collective control and the tail rotor pedal control. The forces and moments applied on the five subsystems as well as the interaction between them are computed and considered as the inputs to the rigid body dynamics block (see figure 2.30).

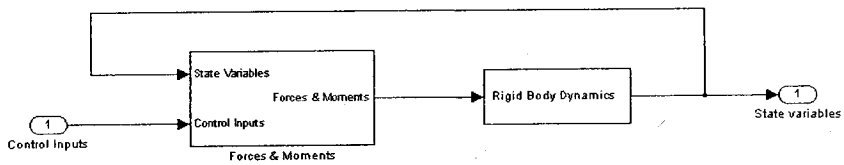

Figure 2.29: Simulation structure

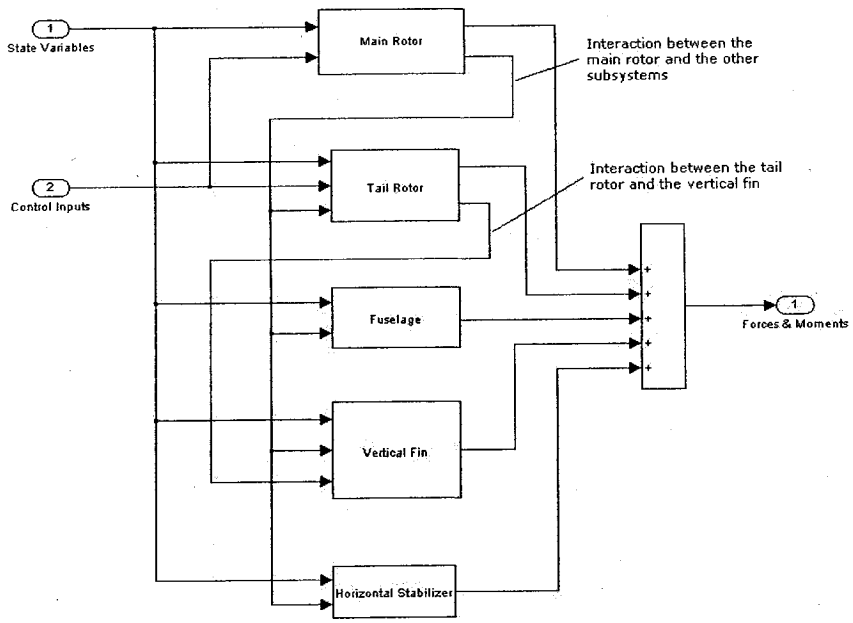

Figure 2.30: Forces and moments block

2.8.2 Flight Experiments

The method used in this thesis to validate the model is to compare flight test data with the simulation results for some certain flight maneuvers in the time domain. The flight test data are taken from the experiment for a YAMAHA R-50 small-size unmanned helicopter done by Mettler et. al. [26].

It should be pointed out that in [26], a linear model is obtained by system identification techniques. Compared to the linear model, the nonlinear model described in this thesis has the advantages of being accurate not only in small regions around equilibrium points but also in more complex flight envelopes.

Description of the Helicopter

The YAMAHA R-50 helicopter [26] (figure 2.31[7]) used in the experiment is a commercially available small-size helicopter originally designed for remote operated crop-dusting. Because of the adequate payload (20 Kg) and the general ease of operation, it has become a choice for research in autonomous flight.

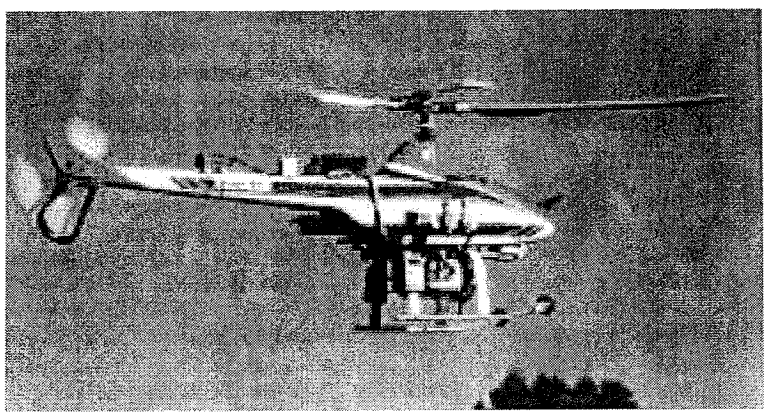

Figure 2.31: The YAMAHA R-50 helicopter

The YAMAHA R-50 uses a two-bladed main rotor with a Bell-Hiller stabilizer bar. The Bell-Hiller stabilizer bar is a secondary rotor consisting of a pair of paddles

[7]Figure 2.31 is taken from [26].

connected to the rotor shaft through an unrestrained teetering hinge. It receives the same cyclic control input as the main rotor but, due to its different design, it has a slower response than the main blades and is also less sensitive to airspeed and wind gusts.

The parameters of the YAMAHA R-50 are listed in table 2.2.

Experimental Setup

For the collection of flight-data from the experiments done by Mettler et. al. [26], the flight maneuvers were commanded by the pilot via the remote control (RC) unit. To ensure the usability of experiment data, it is important to conduct the flight experiments in open-loop. This was possible for all axes except yaw for which an active yaw damping system is in use for the YAMAHA R-50 helicopter. Because of the use of this artificial yaw damping system during the flight experiments, the yaw damping dynamics are taken into account. In this thesis, the augmented yaw dynamics are modeled as first order bare airframe dynamics with a yaw rate feedback as

$$\dot{r} = -K_r r + \frac{(I_{xx} - I_{yy})}{I_{zz}} pq + \frac{I_{xz}}{I_{zz}}(\dot{p} - rq) + \frac{N}{I_{zz}} \tag{2.175}$$

where K_r is the damping coefficient. Three series of experiments were conducted for the hover operating point [26]. In each experiment, the pilot applies a control sequence to one of the control inputs: the main rotor longitudinal control, the main rotor lateral control and the tail rotor pedal control. At the same time, the rest of the control inputs are kept constant and equal to the values in hover. The responses of the helicopter physical variables under these maneuvers are recorded for validation purposes.

Table 2.2: The YAMAHA R-50 helicopter parameters

$m = 97.85$	helicopter weight $(lb \cdot s)$
$I_{xx} = 1.4668$	rolling moment of inertia $(slug \cdot ft^2)$
$I_{yy} = 4.5765$	pitching moment of inertia $(slug \cdot ft^2)$
$I_{zz} = 4.4070$	yawing moment of inertia $(slug \cdot ft^2)$
$I_\beta = 0.86754$	flapping moment of inertia $(slug \cdot ft^2)$
$\Omega = 91.106$	nominal main rotor speed (rad/sec)
$R = 5.05$	main rotor radius (ft)
$c = 0.354$	main rotor chord (ft)
$a = 6.0$	main rotor blade lift curve slope $(1/rad)$
$l_m = 0.21$	main rotor hub location behind c.g. (ft)
$C_{d0} = 0.010$	main rotor blade zero lift drag coefficient
$h_m = 1.841$	main rotor hub height above c.g. (ft)
$\sigma = \frac{2c}{\pi R}$	main rotor solidity ratio
$K_\beta = 73.44$	hub torsional stiffness $(ft \cdot lb/rad)$
$l_t = 6.0425$	tail rotor hub location behind c.g. (ft)
$R_t = 0.853$	tail rotor radius (ft)
$a_t = 3.0$	tail rotor blade lift curve slope $(1/rad)$
$C_{d0t} = 0.010$	tail rotor blade zero lift drag coefficient
$h_t = 0.4747$	tail rotor height above c.g. (ft)
$c_t = 0.1458$	tail rotor chord (ft)
$\Omega_t = 565.49$	nominal tail rotor speed (rad/sec)
$\sigma_t = \frac{2c_t}{\pi R_t}$	tail rotor solidity ratio
$l_h = 3.2925$	stabilizer location behind c.g. (ft)
$C_h = 3.0$	horizontal stabilizer lift curve slope $(1/rad)$
$S_h = 0.6458$	horizontal stabilizer area (ft^2)
$C_v = 2.0$	vertical fin lift curve slope $(1/rad)$
$S_v = 0.3438$	effective vertical fin area (ft^2)
$\epsilon_v = 0.2$	fraction of vertical fin area exposed to tail rotor induced velocity
$S_{xf} = 2.322$	frontal fuselage drag area (ft^2)
$S_{yf} = 7.849$	side fuselage drag area (ft^2)
$S_{zf} = 6.960$	vertical fuselage drag area (ft^2)

2.8.3 Comparison of Simulation and Experimental Data

This section compares simulation results with flight test data from three experiments.

Experiment 1: Main Rotor Longitudinal Control Input

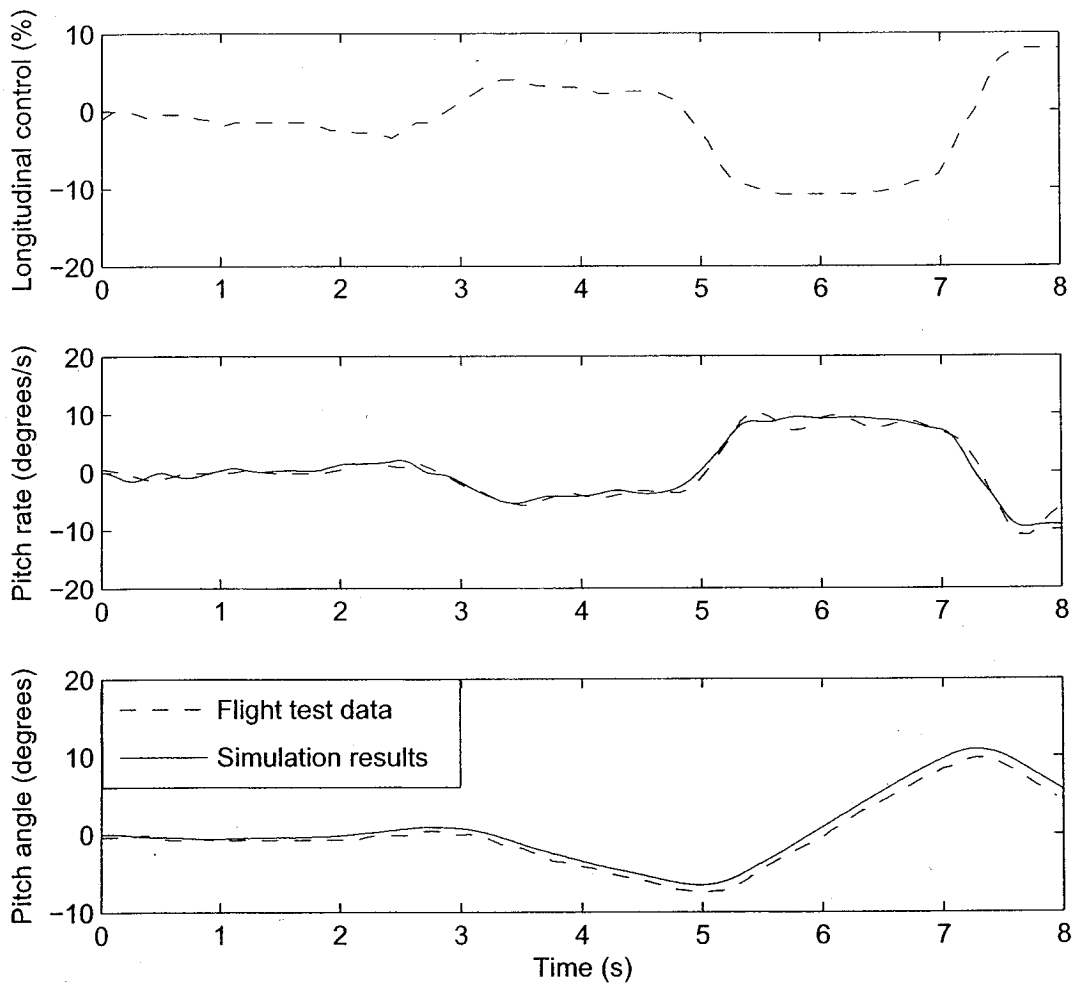

Figure 2.32: Time domain validation for the main rotor longitudinal control input

In this experiment, the pilot applies a control sequence to the main rotor longitudinal control input as shown in figure 2.32. The other control inputs are kept constant. The control input is represented by the percentage of the maximum input

the pilot can apply. A positive (negative) value corresponds to the pilot pushing the cyclic stick forward (pulling the cyclic stick backward). This will cause the helicopter to experience a nose-down (nose-up) motion.

Figure 2.32 shows the pitch rate and pitch angle responses of the helicopter recorded by flight test data (dashed line) and predicted by model simulation (solid line). It can be seen that a good agreement between them is achieved except for a small amount of mismatch. From $5.3s$ to $7s$, the flight data show some small oscillations in pitch rate while the simulation results do not show this effect. The small mismatch might be due to the approximate way the artificial yaw dynamics are modeled and the likely omission of some minor aerodynamic effects.

Experiment 2: Main Rotor Lateral Control Input

In this experiment, the pilot applies a control sequence to the main rotor lateral control input as shown in figure 2.33. The other control inputs are kept constant. The control input is represented by the percentage of the maximum input the pilot can apply. A positive value corresponds to the pilot pushing the cyclic stick to the right (left). This will cause the helicopter to roll to the right (left).

Figure 2.33 shows the roll rate and roll angle responses of the helicopter recorded by flight test data and predicted by model simulation. Similar to experiment 1, a good agreement between them is shown except for a small amount of mismatch. From $2.2s$ to $2.8s$, $4s$ to $5.5s$ and $6s$ to $8s$ the flight data show some small oscillation in roll rate while the simulation results do not show the same effect. The mismatch might also be due to the approximate way the artificial yaw dynamics are modeled and the likely omission of some aerodynamic effects.

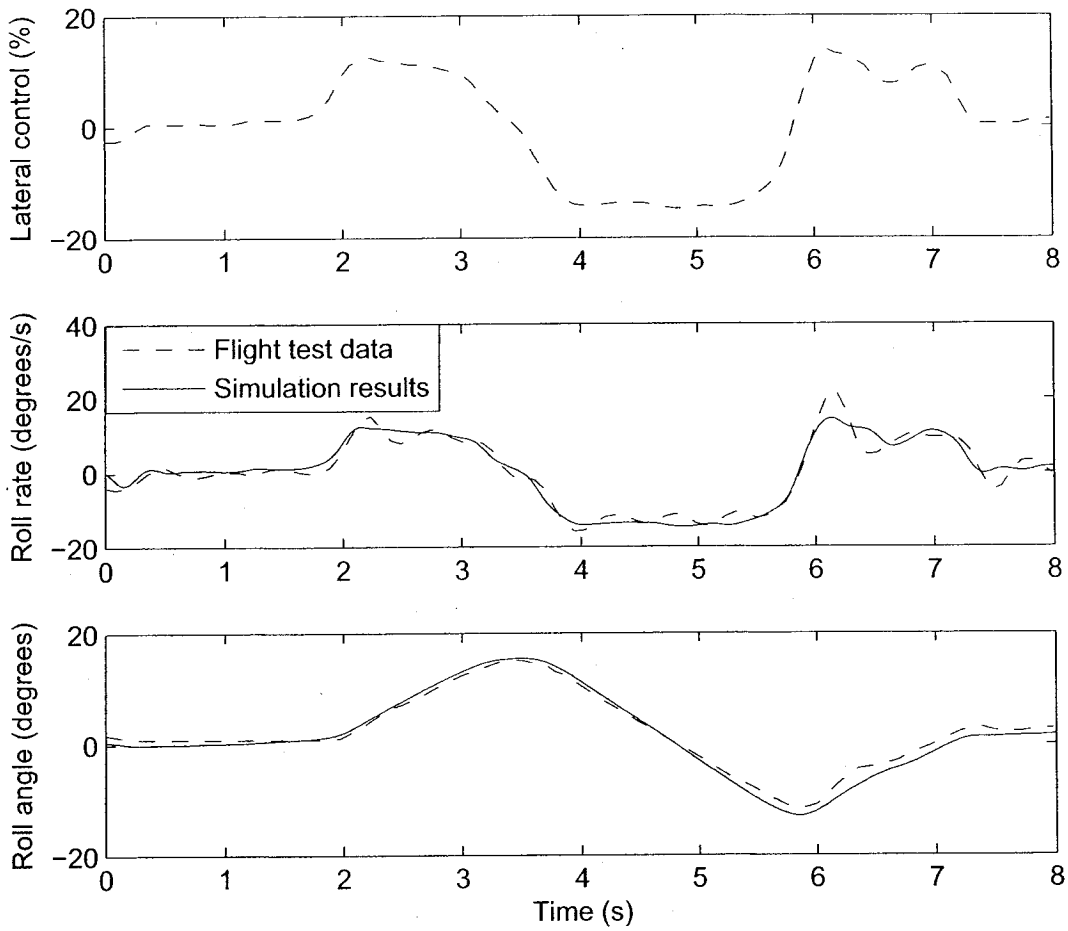

Figure 2.33: Time domain validation for the main rotor lateral control input

Experiment 3: Tail Rotor Pedal Control Input

In this experiment, the pilot applies a control sequence to the tail rotor pedal control input as shown in figure 2.34. The other control inputs are kept constant. The control input is represented by the percentage of the maximum input the pilot can apply. A positive value corresponds to the pilot stepping on the right (left) pedal. This will cause the helicopter to yaw to the right (left).

Figure 2.34 shows the yaw rate and yaw angle responses of the helicopter recorded by flight test data and predicted by model simulation. The results show a good

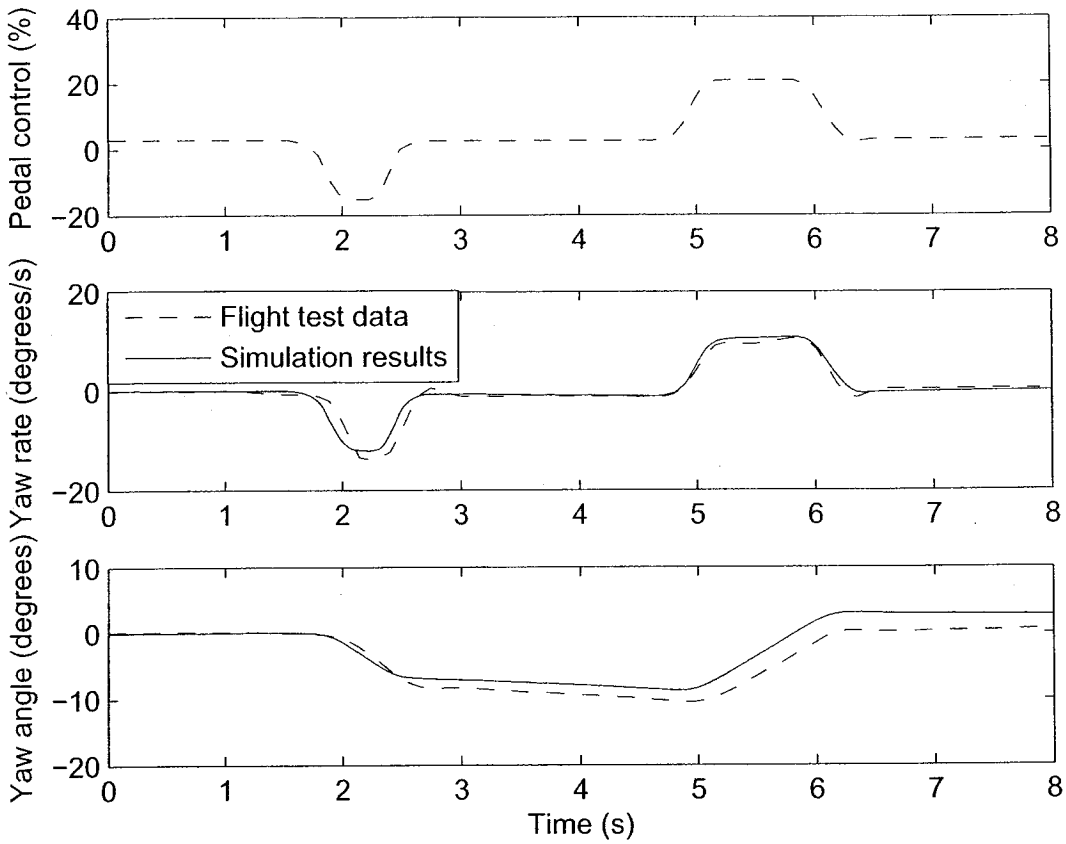

Figure 2.34: Time domain validation for the tail rotor pedal control input

agreement. However, during $1.8s$ to $2.7s$ the yaw rate response has approximately 0.1 seconds of delay relative to the flight data. This small mismatch is accounted for by the artificial yaw damping system. Better results could be obtained if the yaw damping system was disabled during the flight experiments or if the actual actuator inputs were measured.

Chapter 3

Piecewise-Affine Controller Design

In this chapter a simplified three degree of freedom helicopter model is derived from the six degree of freedom model described in chapter 2. A PWA controller will then be designed for this three degree of freedom model. This PWA controller for the lateral plane can be used in conjunction with another controller for the longitudinal plane to control the six degree of freedom helicopter. However, the design of the controller for the longitudinal plane does not follow under the scope of this thesis.

3.1 Simplified Three Degree of Freedom Model

To derive the equations of motion of the three degree of freedom model, it will be assumed that the motion of the helicopter is restricted to the lateral plane. Therefore, the equations of motion can be derived from the equations (2.32) by setting the longitudinal variables to zero, i.e. $w = 0, p = 0, q = 0, \phi = 0, \theta = 0$, yielding

$$\dot{u} = vr + \frac{X}{m} \tag{3.1}$$

$$\dot{v} = -ur + \frac{Y}{m} \tag{3.2}$$

$$\dot{r} = \frac{N}{I_{zz}} \tag{3.3}$$

$$\dot{\psi} = r \tag{3.4}$$

where X, Y and N are the external forces and moments applied on the helicopter and can be written as (refer to equation (2.33))

$$X = X_m + X_f \tag{3.5}$$

$$Y = Y_m + Y_t + Y_v + Y_f \tag{3.6}$$

$$N = N_m + N_t + N_v \tag{3.7}$$

Substituting equations for X_m, Y_m, Y_t, Y_v, N_m, N_t and N_v (see sections 2.2 - 2.6) into equations (3.5) - (3.7) yields

$$X = T_m \sin a_1 + X_f \tag{3.8}$$

$$Y = T_m \sin b_1 + T_t + Y_v + Y_f \tag{3.9}$$

$$N = Q_m - T_t l_t + Y_v l_v \tag{3.10}$$

Substituting into equations (3.1) - (3.4) yields

$$\dot{u} = vr + \frac{T_m \sin a_1 + X_f}{m} \tag{3.11}$$

$$\dot{v} = -ur + \frac{T_m \sin b_1 + T_t + Y_v + Y_f}{m} \tag{3.12}$$

$$\dot{r} = \frac{Q_m - T_t l_t + Y_v l_v}{I_{zz}} \tag{3.13}$$

$$\dot{\psi} = r \tag{3.14}$$

This simplified model will be further modified for control purposes in the next section.

3.2 Control Objective and Model Description

As shown in figure 3.1, the motion of the helicopter will be restricted to the lateral plane. The control objective is to design a controller that forces the helicopter to follow the straight line $y = 0$ with a constant velocity u_0. The model of the three

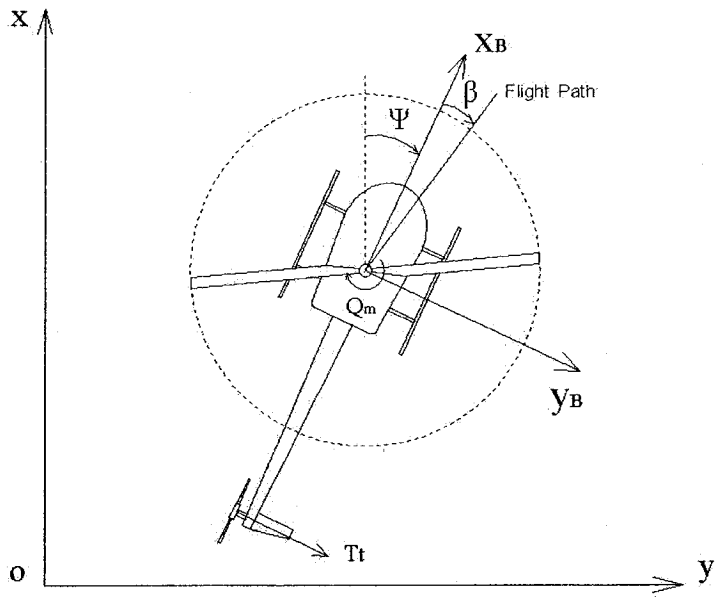

Figure 3.1: Three degree of freedom helicopter model

degree of freedom helicopter is described in the last section. Note that in equations (3.8) - (3.10) T_m, T_t, Y_v, Q_m, X_f and Y_f are highly nonlinear functions of the state variables and control inputs, and since the difficulty of performing PWA controller synthesis depends on the number of variables in the domain of the nonlinearity, some further assumptions will be made to reduce the number of variables in the domain of the nonlinearity to two. Although this will increase the conservativeness of the model, to the knowledge of the author, it is still a good approximation of three degree of freedom helicopter models and appropriate for PWA controller design.

The assumptions are as follows.

1. The advance ratio (forward speed/blade tip speed: $u/\Omega R$) is small. Therefore the forces and moments generated by the fuselage are neglected.

2. The moment around the z_B-axis generated by the vertical fin is simplified and regarded as a damper. It can be written as

$$N_v = -k_r r \tag{3.15}$$

3. The main rotor and tail rotor thrusts are simplified and described as

$$T_m = k_m \delta_{col} \tag{3.16}$$

$$T_t = k_t \delta_{ped} \tag{3.17}$$

where k_m and k_t are the blade constants, δ_{col} and δ_{ped} are the main rotor longitudinal cyclic control and the tail rotor pedal control, respectively.

4. The rotor torque is described as

$$Q_m = \lambda_m \delta_{col} \tag{3.18}$$

5. Assume that another controller for the main rotor has been designed to implement the following functions:

   - The thrust T_m remains constant by keeping the main rotor collective control δ_{col} constant (see equation (3.16)).
   - The forward speed of the helicopter is kept constant (u_0) by changing the longitudinal flapping a_1.
   - The overall force component along the y_B-axis is kept equal to $k_v v$ by changing the lateral flapping b_1, where k_v is damping coefficient and v is

the side velocity of the helicopter.

$T_m = k_m\delta_{col}$, $T_t = k_t\delta_{ped}$, $Q_m = \lambda_m\delta_{col}$, $N_v = -k_r r$ According to these assumptions equations (3.11) - (3.14) transform to

$$\dot{u} = 0 \tag{3.19}$$

$$\dot{v} = -u_0 r - \frac{k_v v}{m} \tag{3.20}$$

$$\dot{r} = -\frac{k_r r}{I_{zz}} + \frac{Q_m}{I_{zz}} - \frac{k_t l_t \delta_{ped}}{I_{zz}} \tag{3.21}$$

$$\dot{\psi} = r \tag{3.22}$$

For control purposes, the equation for velocity on the y_B-axis is added as

$$\dot{y} = u_0 \sin(\psi + \beta) + v\cos(\psi + \beta) \tag{3.23}$$

Collecting equations (3.20) - (3.23) the helicopter lateral dynamics can be written in matrix form as

$$\begin{bmatrix} \dot{\psi} \\ \dot{r} \\ \dot{v} \\ \dot{y} \end{bmatrix} = \begin{bmatrix} 0 & 1 & 0 & 0 \\ 0 & -\frac{k_r}{I_{zz}} & 0 & 0 \\ 0 & -u_0 & -\frac{k_v}{m} & 0 \\ 0 & 0 & 0 & 0 \end{bmatrix} \begin{bmatrix} \psi \\ r \\ v \\ y \end{bmatrix} + \begin{bmatrix} 0 \\ \frac{Q_m}{I_{zz}} \\ 0 \\ g(\psi, v) \end{bmatrix} + \begin{bmatrix} 0 \\ -\frac{k_t l_t}{I_{zz}} \\ 0 \\ 0 \end{bmatrix} u \tag{3.24}$$

$$g(\psi, v) = u_0 \sin(\psi + \beta) + v\cos(\psi + \beta) \tag{3.25}$$

$$\beta = \arctan\frac{v}{u_0} \tag{3.26}$$

where ψ is the heading angle with time derivative r, k_t is the blade constant of the tail rotor, λ_m is the main rotor torque constant, k_r and k_v are the damping coefficients and u is the control input ($u = \delta_{ped}$). Assume that the helicopter can start from any possible initial heading angle and any initial point in the domain $y \in [-10, 10]$. Note that the nonlinearities $\sin\psi$ and $\cos\psi$ are introduced by the heading angle ψ, which

can start from any initial angle. Therefore the full nonlinear equations have to be taken into account.

The controller design method proposed in this thesis consists of two steps summarized in figure 3.2 [34]. The first step is to create a partition of the state space

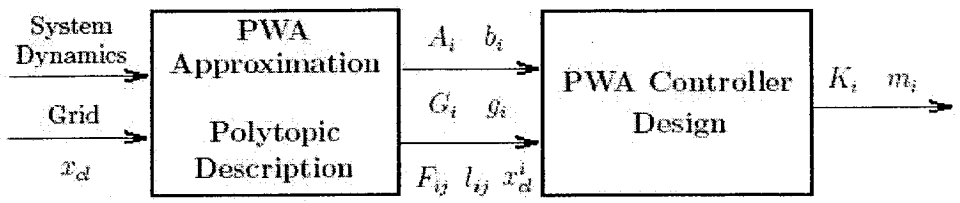

Figure 3.2: The PWA controller design method

into a finite number of polytopic cells and a PWA approximation for the nonlinear system by giving the system dynamics, the desired closed-loop equilibrium point x_{cl} and a uniform rectangular grid for the domain of the nonlinearity. The parameters describing the partition and the approximation are then used to design a PWA controller for the system, described by the parameters K_i and m_i in each region $\mathcal{R}$. The next two sections will explain the PWA approximation and PWA controller design, respectively.

3.3 PWA Approximation

PWA systems are able to approximate with high accuracy a large class of nonlinear dynamical systems of the following form [36]

$$\begin{bmatrix} \dot{x} \\ \dot{z} \end{bmatrix} = \begin{bmatrix} A_{xx} & A_{xz} \\ A_{zx} & A_{zz} \end{bmatrix} \begin{bmatrix} x \\ z \end{bmatrix} + \begin{bmatrix} b_x \\ f(x,z) \end{bmatrix} + B(x,z)u \tag{3.27}$$

$$y = C \begin{bmatrix} x \\ z \end{bmatrix} \tag{3.28}$$

where $b_x \in R^{n_x}$ is a constant vector, $x \in R^{n_x}$ contains the state variables with affine dynamics, and $z \in R^{n_z}$ contains the state variables associated with the nonlinear dynamics. These variables will be stacked together in the vector $w = [x^T \quad z^T]^T$. The function $f(x, z)$ is the nonlinear function. The vector $u \in R^{n_u}$ is the control input.

It is easy to see that the helicopter dynamics (equation (3.24)) is in this form. To approximate the nonlinear function $g(\psi, v)$ by a PWA function, the space of variables in the domain of the nonlinearity should be partitioned into simplicial[1] cells. In each cell, the PWA approximation considered in this thesis is the hyperplane that passes through the values of the function at the vertices of the cell. The algorithm for computing the PWA approximation consists of the following steps [36]:

1. Given a rectangular grid for the domain of the nonlinearity, order all vertices of that grid.

2. Group the vertices into simplicial cells.

3. Find a polytopic description for each cell.

4. Find a parametric description for the boundaries.

5. Find the PWA approximation of the nonlinearity and the piecewise-constant approximation of the input matrix within each cell.

The algorithm is described in detail in [36]. After the function $g(\psi, v)$ from the nonlinear system (3.24) is replaced by its PWA approximation, the result will be a PWA system as follows.

$$\dot{x}(t) = A_i x(t) + a_i + B_i u(t), \text{ if } x(t) \in \mathcal{R}_i \tag{3.29}$$

where $x(t) \in \mathbb{R}^n$, $u(t) \in \mathbb{R}^m$, $y(t) \in \mathbb{R}^p$. The polytopic cells, $\mathcal{R}_i$, $i \in \mathcal{I} = \{1, \ldots, M\}$,

[1] A simplex in $\mathbb{R}^n$ is defined as the convex hull of $n + 1$ affinely independent points. The convex hull of a set $\mathcal{S}$ is the smallest convex set that contains $\mathcal{S}$. For example, a simplex in $\mathbb{R}^2$ is a triangle.

partition a subset of the state space $\mathcal{X} \subset \mathbb{R}^n$ such that $\cup_{i=1}^{M} \overline{\mathcal{R}}_i = \mathcal{X}$, $\mathcal{R}_i \cap \mathcal{R}_j = \emptyset$, $i \neq j$, where $\overline{\mathcal{R}}_i$ denotes the closure of $\mathcal{R}_i$. Each cell is constructed as the intersection of a finite number of half spaces

$$\mathcal{R}_i = \{x \mid \bar{G}_i \bar{x} \succ 0\} \tag{3.30}$$

where

$$\bar{G}_i = [G_i \quad g_i], \quad \bar{x} = \begin{bmatrix} x \\ 1 \end{bmatrix}$$

and $\bar{G}_i \in \mathbb{R}^{p_i \times (n+1)}$.

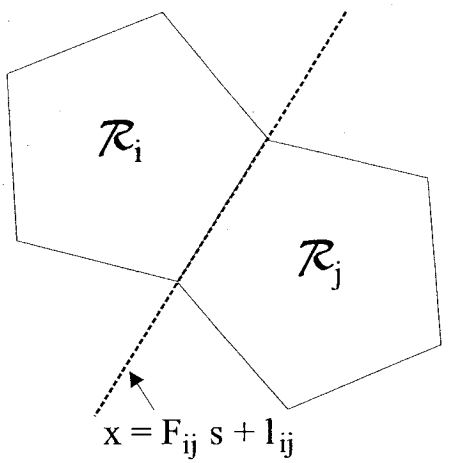

Figure 3.3: Polytopic regions $\mathcal{R}_i$ and $\mathcal{R}_j$ and boundary

Each polytopic cell has a finite number of facets and vertices. Any two cells sharing a common facet will be called *level-1* neighboring cells. Any finite number of cells sharing a common vertex will be called *level-2* neighboring cells. Let $\mathcal{N}_i = \{$*level-1* neighboring cells of $\mathcal{R}_i\}$. It is also assumed that a parametric description of the boundaries can be obtained as (see figure 3.3[2])

$$\overline{\mathcal{R}_i} \cap \overline{\mathcal{R}_j} \subseteq \{F_{ij} s + l_{ij} \mid s \in \mathbb{R}^{n-1}\} \tag{3.31}$$

[2]Figure 3.3 is taken from the picture in [34].

for $i = 1, \ldots, M$, $j \in \mathcal{N}_i$, where $F_{ij} \in \mathbb{R}^{n \times (n-1)}$ is a full rank matrix and $l_{ij} \in \mathbb{R}^n$.

For the grid chosen to approximate the nonlinear function, ψ and v take the values $\{-\frac{\pi}{2}, -\frac{\pi}{6}, -\frac{\pi}{20}, \frac{\pi}{20}, \frac{\pi}{6}, \frac{\pi}{2}\}$ and $\{-0.8, -0.01, 0.01, 0.8\}$ respectively. The domain of the nonlinearity is therefore divided into 30 simplicial cells as shown in figure 3.4.

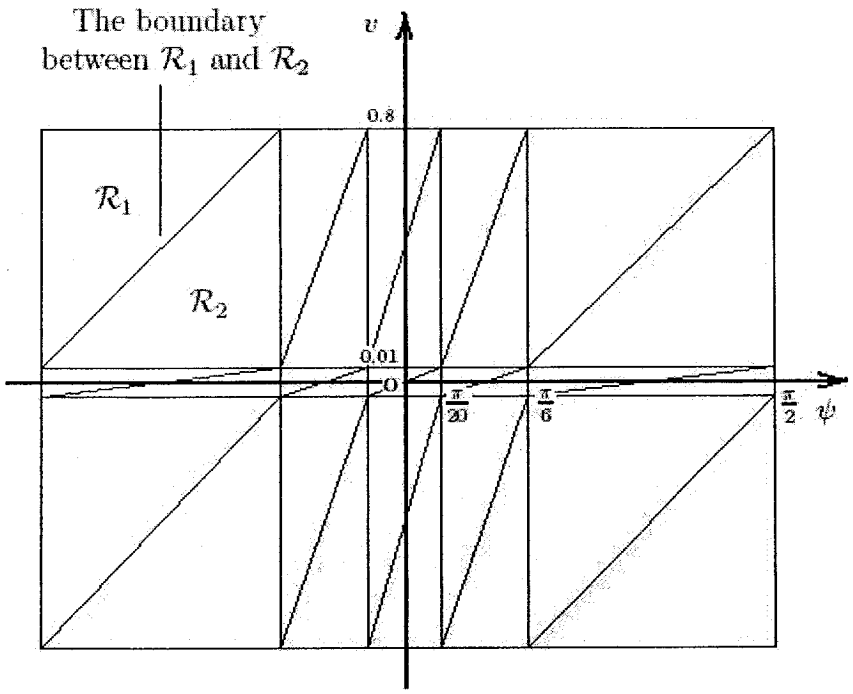

Figure 3.4: Simplicial cells

3.4 PWA Controller Design

The goal is to design a control input of the following form to stabilize the equilibrium point $x_{cl} = [0 \quad 0 \quad 0 \quad 0]^T$ for the system.

$$u = \bar{K}_i \bar{x}, x \in \mathcal{R}_i \tag{3.32}$$

where

$$\bar{K}_i = [K_i \quad m_i], \quad \bar{x} = \begin{bmatrix} x \\ 1 \end{bmatrix}$$

Substitution of equation (3.32) into equation (3.29) yields the dynamics of the closed-loop system.

$$\dot{\bar{x}} = (\bar{A}_i + \bar{B}_i \bar{K}_i)\bar{x}, \quad \text{if } x \in R \tag{3.33}$$

where $\bar{A}_i \in \mathbb{R}^{(n+1)\times(n+1)}$ and $\bar{B}_i \in \mathbb{R}^{(n+1)\times m}$ are defined as

$$\bar{A}_i = \begin{bmatrix} A_i & a_i \\ 0 & 0 \end{bmatrix}, \quad \bar{B}_i = \begin{bmatrix} B_i \\ 0 \end{bmatrix}$$

A Lyapunov (or energy-like) function [14][44] based method is used to design the controller. The candidate Lyapunov function will be piecewise quadratic.

$$V(x) = \sum_{i=1}^{M} \beta_i(x) V_i(x) \tag{3.34}$$

where

$$\beta_i(x) = \begin{cases} 1, & x \in \mathcal{R}_i \\ 0, & x \in \mathcal{R}_j, \ j \neq i \end{cases}, \tag{3.35}$$

for $i = 1, \ldots, M$ and $V_i(x)$ is quadratic of the form

$$V_i(x) = \bar{x}^T \bar{P}_i \bar{x} \tag{3.36}$$

with $\bar{P}_i$ defined as

$$\bar{P}_i = \begin{bmatrix} P_i & -P_i x_{cl} \\ -x_{cl}^T P_i^T & r_i \end{bmatrix} \tag{3.37}$$

where $P_i = P_i^T > 0$, $P_i \in \mathbb{R}^{n\times n}$, $r_i \in \mathbb{R}$ and therefore $\bar{P}_i = \bar{P}_i^T \in \mathbb{R}^{(n+1)\times(n+1)}$. In our

case, because $x_{cl} = [0 \quad 0 \quad 0 \quad 0]$, we have

$$\bar{P}_i = \begin{bmatrix} P_i & 0 \\ 0 & r_i \end{bmatrix} \tag{3.38}$$

To design a stabilizing controller for the PWA system, we want to satisfy the following constraints [37][38]:

1. *Continuity of the control input* - In order to enforce continuity of the control input at the boundaries, we want

$$u_i(x) = u_j(x) \text{ for } x \in \bar{\mathcal{R}}_i \cap \bar{\mathcal{R}}_j,$$

$$\text{i.e. } \bar{K}_i \bar{x} = \bar{K}_j \bar{x} \text{ for } x = F_{ij} s + l_{ij} \text{ or } \bar{x} = \bar{F}_{ij} \bar{s}$$

Therefore, we have the following constraint in each region:

$$(\bar{K}_i - \bar{K}_j)\bar{F}_{ij} = 0, \quad \text{for } j \in \mathcal{N}_i \tag{3.39}$$

where

$$\bar{F}_{ij} = \begin{bmatrix} F_{ij} & l_{ij} \\ 0 & 1 \end{bmatrix}$$

2. *Continuity of the candidate Lyapunov function* - Continuity of the candidate Lyapunov function across the boundaries in each region is enforced by

$$V_i(x) = V_j(x) \text{ for } x \in \bar{\mathcal{R}}_i \cap \bar{\mathcal{R}}_j,$$

or

$$\bar{x}^T \bar{P}_i \bar{x} = \bar{x} \bar{P}_j \bar{x} \text{ for } \bar{x} = \bar{F}_{ij} \bar{s}$$

This implies

$$\bar{F}_{ij}^T(\bar{P}_i - \bar{P}_j)\bar{F}_{ij} = 0 \tag{3.40}$$

3. *Positive definiteness of the candidate Lyapunov function* - The candidate Lyapunov function is positive definite if it satisfies the inequality:

$$V_i(x) > 0, \forall x \in \mathcal{R}_i,\ x \neq x_{cl} \tag{3.41}$$

Using the polytopic description of the cells (equation (3.30)) and the $\mathcal{S}-$procedure [1], it can be shown [38] that sufficient conditions for satisfying the above inequality for each region $\mathcal{R}_i$ are the existence of $\bar{P}_i$ and matrix Z_i with nonnegative entries satisfying

$$\bar{P}_i - \check{E}_i^T Z_i \check{E}_i > 0 \tag{3.42}$$

where $\check{E}_i = [G_i \quad g_i]$.

4. *Decrease of the candidate Lyapunov function over time* - The candidate Lyapunov function is decreasing over time if it satisfies the inequality

$$\frac{dV}{dt} \leq -\alpha V(x) \tag{3.43}$$

Sufficient conditions for satisfying the inequality (3.43) for each region $\mathcal{R}_i$ are the existence of matrices $\Lambda_i,\ i = 1, \ldots, n$ with nonnegative entries satisfying (see [38] for details)

$$\bar{P}_i\bar{A}_i + \bar{A}_i^T\bar{P}_i + \alpha\bar{P}_i + \check{E}_i^T\Lambda_i\check{E}_i < 0 \tag{3.44}$$

Our controller design consists of the following steps [38][40]:

1. *Linear controller design* - Design a linear local controller to achieve the de-

sired closed-loop dynamics in the region where the closed-loop equilibrium point ($x_{cl} = [0 \quad 0 \quad 0 \quad 0]^T$) is located. To do this, consider dynamics of the system in this region described by

$$\dot{x}(t) = A_{i^*}x(t) + a_{i^*} + B_{i^*}u(t), \quad \text{if } x(t) \in \mathcal{R}_{i^*} \tag{3.45}$$

We assume that there exists a vector m_{i^*} which satisfies

$$A_{i^*}x_{cl} + a_{i^*} + B_{i^*}m_{i^*} = 0 \tag{3.46}$$

Now using the control input

$$u(t) = K_{i^*}x(t) + m_{i^*} \quad , \tag{3.47}$$

the closed-loop dynamics of the system in the region where the equilibrium point lies are given by

$$\dot{x}(t) = A_{i^*} + B_{i^*}K_{i^*}x(t) \tag{3.48}$$

The matrix gain K_{i^*} can then be designed using linear control methodologies to satisfy desired design objectives for either stability or performance. In this thesis, an LQR controller is designed using the following weighting parameters.

$$Q = \begin{bmatrix} 50 & 0 & 0 & 0 \\ 0 & 500 & 0 & 0 \\ 0 & 0 & 500 & 0 \\ 0 & 0 & 0 & 50 \end{bmatrix}, \quad R = 0.5$$

2. *Local quadratic Lyapunov function* - Having a linear state feedback controller gain, K_{i^*}, the following linear matrix inequalities (LMIs) set is solved to find a

quadratic Lyapunov function for the region where the closed-loop equilibrium point is located: $\mathcal{R}_{i^*}$.

$$\begin{aligned} &\text{find} \quad P_{i^*} > 0 \\ &P_{i^*}(A_{i^*} + B_{i^*}K_{i^*}) + (A_{i^*} + B_{i^*}K_{i^*})^T P_{i^*} < 0 \end{aligned} \tag{3.49}$$

The quadratic Lyapunov function is then

$$V_{i^*}(x) = \bar{x}^T \bar{P}_{i^*} \bar{x}, \quad x \in \mathcal{R}_{i^*} \tag{3.50}$$

where

$$\bar{P}_{i^*} = \begin{bmatrix} P_{i^*} & 0 \\ 0 & r_{i^*} \end{bmatrix} \tag{3.51}$$

3. *Uniformity of the closed-loop dynamics* - The closed-loop dynamics of the system in the region where the equilibrium point is located can serve as a reference model for closed-loop dynamics in other regions. Using the method introduced in [40], we try to minimize the upper bound of the difference between the closed-loop dynamics of all regions and that of the region holding the equilibrium point. This bound can be formulated as the following inequality:

$$\| \bar{A}_i + \bar{B}_i \bar{K}_i - (\bar{A}_{i^*} + \bar{B}_{i^*} \bar{K}_{i^*}) \| < \beta \tag{3.52}$$

Using (3.52), the goal is to design a PWA controller and a piecewise quadratic Lyapunov function for system (3.29). To achieve this goal, the following constraints should be satisfied: continuity of the control input (3.39), continuity of the candidate piecewise Lyapunov function (3.40), positive definiteness of the candidate Lyapunov function (3.42) and decrease of the candidate Lyapunov function over time (3.44). Therefore, the problem can be formulated as follows

[40]:

$$
\begin{aligned}
& \min(\beta) \\
\text{s.t.} \quad & \bar{P}_i \equiv \begin{bmatrix} P_i & 0 \\ 0 & r_i \end{bmatrix} \\
& P_i > 0 \\
& (\bar{K}_i - \bar{K}_j)\bar{F}_{ij} = 0, \text{for } j \in \mathcal{N}_i \\
& \bar{F}_{ij}^T(\bar{P}_i - \bar{P}_j)\bar{F}_{ij} = 0, \text{for } j \in \mathcal{N}_i \\
& Z_i \succ 0 \\
& \bar{P}_i - \check{E}_i^T Z_i \check{E}_i > 0 \\
& \Lambda_i \succ 0 \\
& \bar{P}_i(\bar{A}_i + \bar{B}_i\bar{K}_i) + (\bar{A}_i + \bar{B}_i\bar{K}_i)^T\bar{P}_i + \check{E}_i^T\Lambda_i\check{E}_i < 0 \\
& -K_{Lim} \prec \bar{K}_i \prec K_{Lim} \\
& -\beta \prec (\bar{A}_i + \bar{B}_i\bar{K}_i) - (\bar{A}_{i^*} + \bar{B}_{i^*}\bar{K}_{i^*}) \prec \beta \\
& \bar{K}_{i^*} = [K_{i^*} \quad k_{i^*}] \\
& \bar{P}_{i^*} = \begin{bmatrix} P_{i^*} & 0 \\ 0 & r_{i^*} \end{bmatrix} \\
& \text{for } i \in \mathcal{I} = \{1, \ldots, M\}, i \neq i^*
\end{aligned}
\tag{3.53}
$$

where i^* is the index of the region $\mathcal{R}_{i^*}$ containing the equilibrium point x_{cl}. The constraints of the synthesis problem include a set of Bilinear Matrix Inequalities (BMIs). PENBMI [7] is the first available general purpose, non-commercial code for BMIs and it is used to solve (3.53) in this thesis.

If there is a solution to the problem (3.53), the following results can be established to prove stability of the closed-loop system [34].

Theorem 3.4.1 *Assume the Lyapunov function (3.34) is defined in* $\mathcal{X} \subseteq \mathbb{R}^n$. *If*

there is a solution to the design problem (3.53), then the PWA approximate closed-loop system is locally exponentially stable inside any subset of the largest level set of the control Lyapunov function (3.34) that is fully contained in $\mathcal{X}$.

Proof: See [34] for details.

Furthermore, if there is a solution to the design problem (3.53) and if the approximation error between the PWA closed-loop system and the original nonlinear closed-loop system is small enough, then it can be shown that the original closed-loop system is locally exponentially stable inside any subset of the largest level set of the control Lyapunov function (3.34) that is fully contained in $\mathcal{X}$ (see [34] for the formal result).

Chapter 4

Simulation Results

This chapter shows simulation results for the PWA controller developed in the last chapter. The parameters used in the simulation are listed in table 4.1. The simulations were done in MATLAB and SIMULINK version 7.0 and the controller optimization problem was solved using SeDuMi [18] with YALMIP [19].

Table 4.1: Simulation parameters

$I_{zz} = 0.01$	moment of inertia $(Kg \cdot m^2)$
$m = 1$	helicopter mass (Kg)
$l_t = 0.5$	tail rotor hub location behind c.g. (m)
$k_t = 0.01$	blade constant of the tail rotor
$k_r = 0.1$	yaw damping coefficient
$k_v = 1$	slide damping coefficient
$Q_m = 1$	main rotor torque $(N \cdot m)$
$u_0 = 0.7$	helicopter forward velocity (m/s)
$\psi_0 = \frac{\pi}{3}$	initial yaw angle (rad)
$y_0 = 5$	initial lateral position (m)

In the simulation, the three degree of freedom helicopter model is first approximated by a PWA approximate representation and a PWA controller is designed for this approximate model. The developed PWA controller is then applied to the approximate model as well as the original nonlinear model (see figure 4.1).

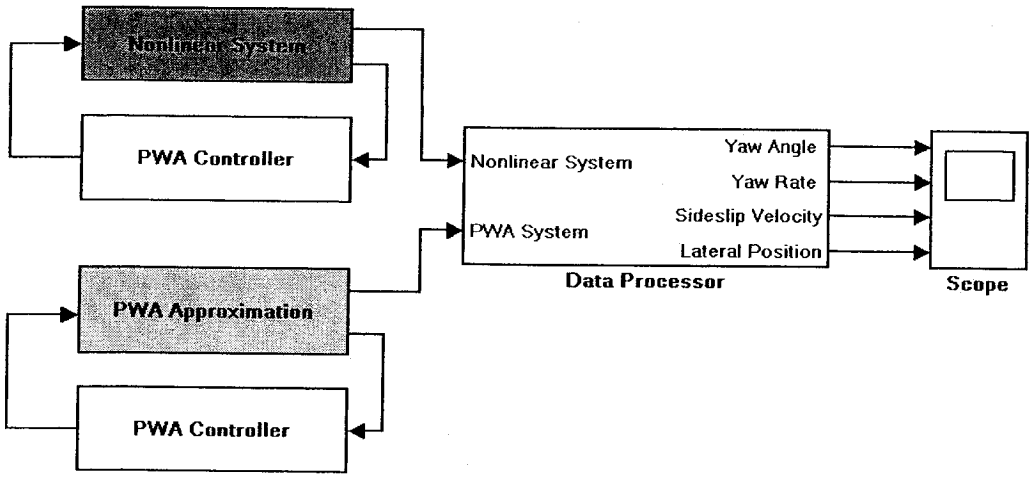

Figure 4.1: Simulink block for the simulation

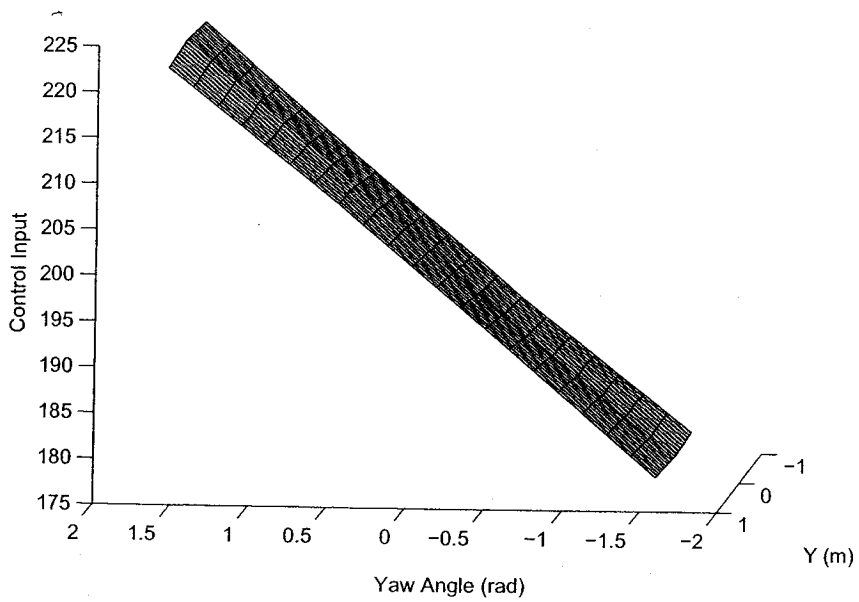

Figure 4.2: PWA control input

Figure 4.2 shows the PWA controller designed for the PWA approximate model. In the domain of the nonlinearity (yaw angle and lateral position), each region $\mathcal{R}_i$ contains an affine controller which is extended from the linear controller in the region where the equilibrium point is located. These controllers together constitute the PWA controller.

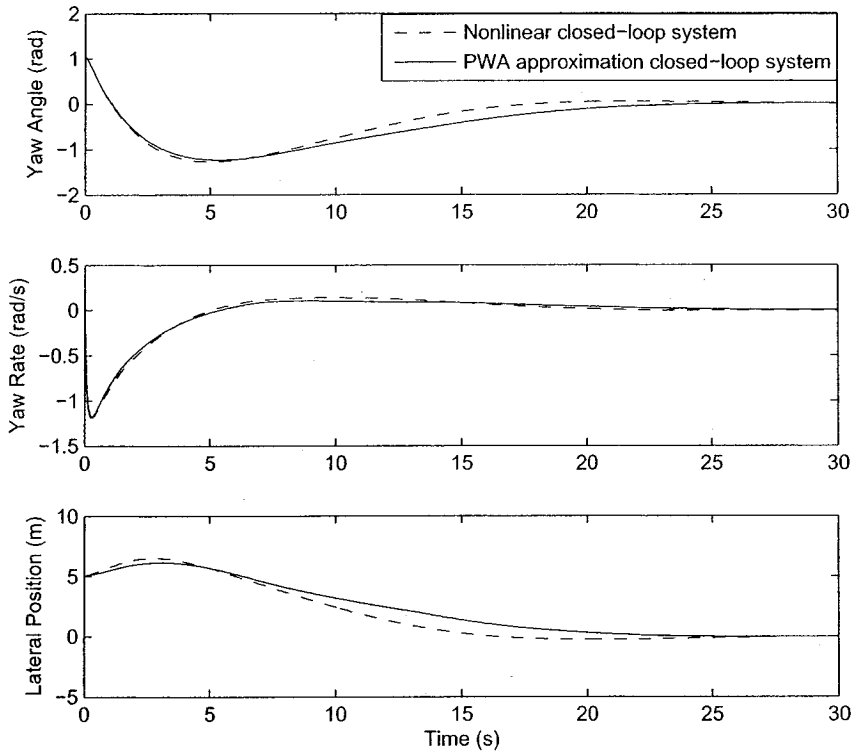

Figure 4.3: Time history of the PWA approximation closed-loop system and that of the nonlinear closed-loop system

Figure 4.3 shows the time history of the PWA approximation closed-loop system (solid line) and that of the nonlinear closed-loop system (dashed line). It can be seen in this simulation that the PWA controller not only stabilized the PWA approximation system, but also stabilized the original nonlinear system. This can also be shown by the trajectory of the nonlinear closed-loop system in the xy plane (figure 4.4). Stability of the closed-loop system is proved by the Lyapunov function shown in

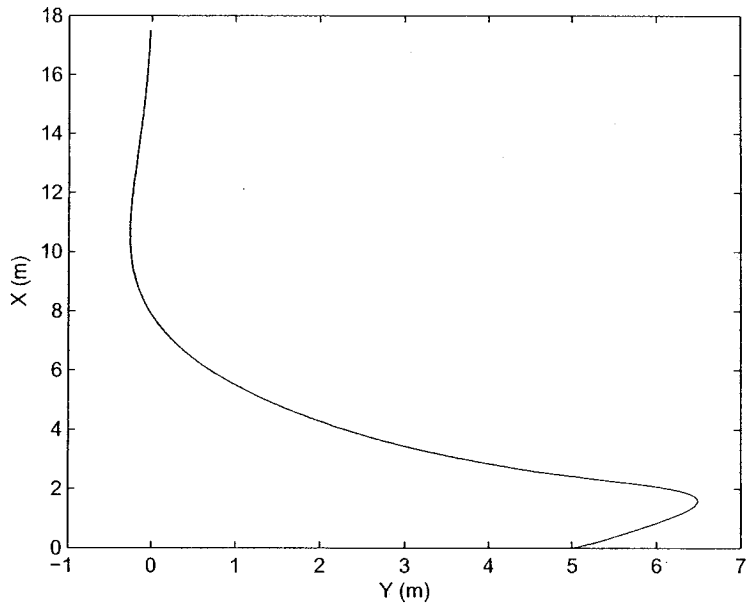

Figure 4.4: x-y trajectory of the closed-loop system with the PWA controller for $\psi_0 = \frac{\pi}{3}, y_0 = 5$

figure 4.5.

Given other initial conditions farther away from the y-axis ($(y_0, \psi_0) \in \{(-3, -80), (-3, -72), (-3, -64), (-3, -56), (-3, -48), (-3, -40), (-3, -32), (-3, -24), (-3, -16), (-3, -8), (3, 8), (3, 16), (3, 24), (3, 32), (3, 40), (3, 48), (3, 56), (3, 64), (3, 72), (3, 80)\}$), simulation results (figure 4.6) show that the nonlinear closed-loop system is also stabilized by the PWA controller.

However, if we apply the linear controller designed for the region where the closed-loop equilibrium point is located to the nonlinear helicopter model, the simulation result is shown in figure 4.7 and figure 4.8. It is easy to see that the linear controller cannot stabilize the system as the PWA controller did.

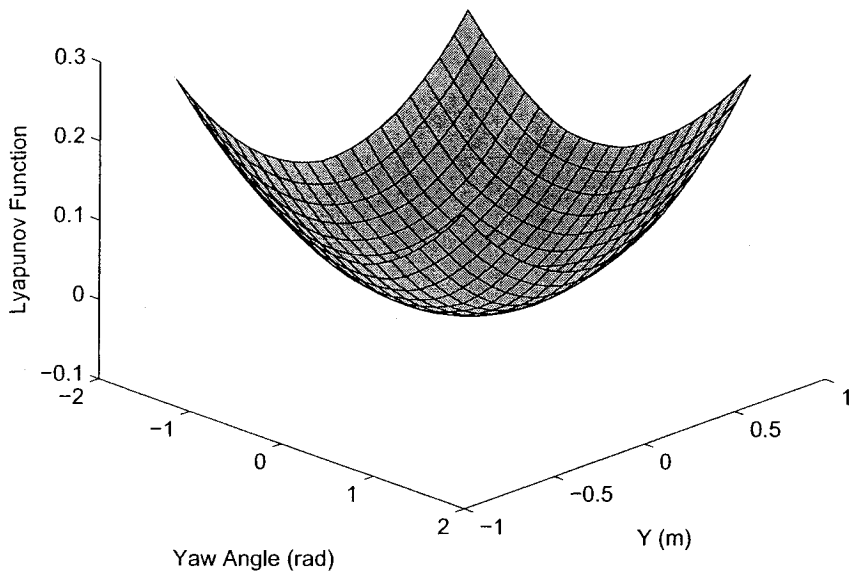

Figure 4.5: Lyapunov function

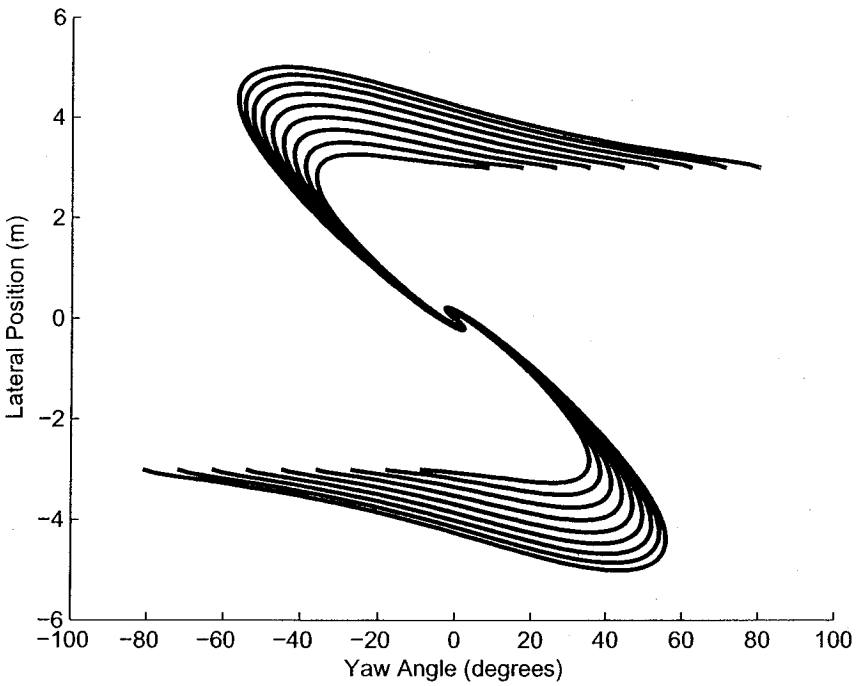

Figure 4.6: Closed-loop system trajectories for different initial conditions

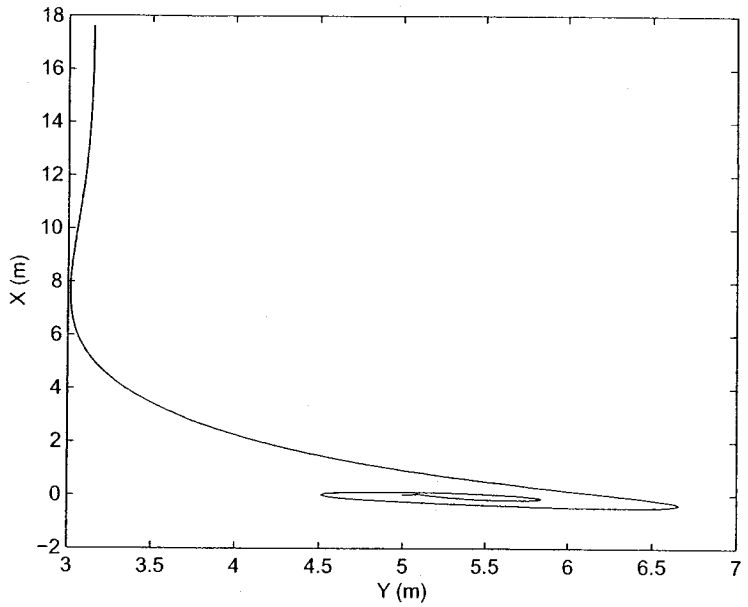

Figure 4.7: x-y trajectory of the closed-loop system with a linear controller for $\psi_0 = \frac{\pi}{3}, y_0 = 5$

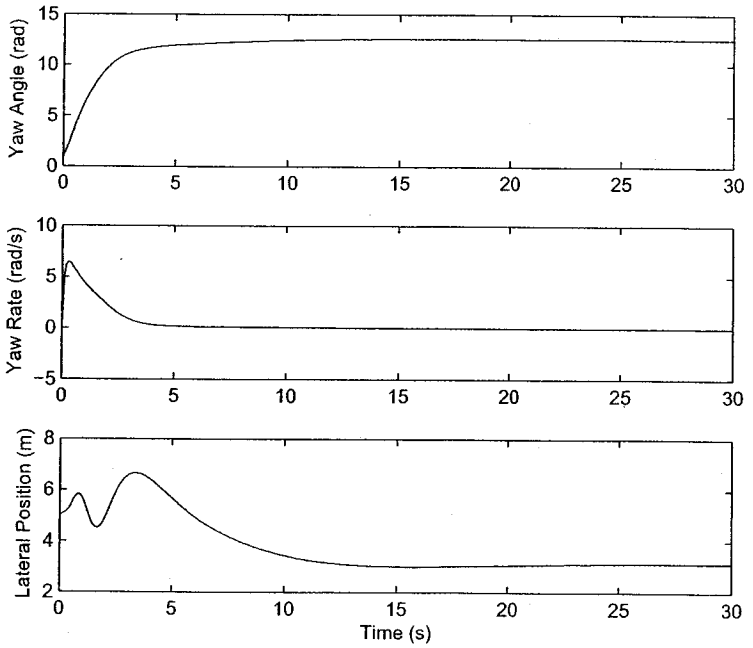

Figure 4.8: Time histories of the closed-loop system with linear a linear controller for $\psi_0 = \frac{\pi}{3}, y_0 = 5$

Chapter 5

Conclusions and Future Work

5.1 Conclusions

In this thesis, a physics based model for aerobatic helicopters was developed. The model was based on a rigid body dynamics formulation with applied external forces and moments including the effects of gravity and aerodynamics. The analysis of the forces and moments followed a component buildup approach. The model was validated by comparing simulation results with flight test data available in the literature for a YAMAHA R-50 helicopter. This model can be used for predicting dynamic performance of aerobatic helicopters and it allows approximations to be made to yield a simplified representation for control design and analysis.

This research presented the first development of a PWA model and controller for an aerobatic helicopter system. The six degree of freedom model developed in this thesis was further simplified to obtain a three degree of freedom helicopter model and a PWA approximate representation. The model was then used to develop a PWA controller for the system. To design this controller the domain of the nonlinearity of the model is first partitioned into simplicial regions and the nonlinear model is approximated by a PWA model. Second, a local linear controller is designed for the approximate model

in the region where the desired closed-loop equilibrium point is located. Furthermore, an optimization problem subject to Bilinear Matrix In- equalities (BMIs) is solved to find a PWA extension of the linear controller. A piecewise quadratic Lyapunov function is then found which proves stability of the closed-loop PWA system.

5.2 Future Work

Future work could be focused on applications of the PWA controller design methodologies to six degree of freedom helicopters. Furthermore, the model described in chapter 2 can be expressed in a linear parameterized form ideal for parameter estimation and adaptive control. Therefore, in alternative, parameter estimation for six degree of freedom helicopters could be implemented in the future by applying flight test data to the linear parameterized model. The following section presents some insight on how this could be done.

5.3 Parameter Estimation

In this section, a method of on-line parameter estimation for the nonlinear helicopter model from chapter 2 is presented theoretically, following the methodology explained in [44].

5.3.1 Helicopter Model with Unknown Parameters

In this section we will present a six degree of freedom nonlinear helicopter model with unknown parameters. This parametric model is based on the one described in chapter 2. An assumption is made that the advance ratio of the helicopter is low ($\frac{u}{\Omega R}$ is small). This assumption will make the parametric model simple and the feasibility of this method is also guaranteed because experiments for low advance ratio flight of

helicopters are not difficult to implement.

Main Rotor Forces and Moments

In low advance ratio flight, the main rotor thrust and torque can be approximated as

$$T_m = m_1 \delta_{col} \tag{5.1}$$

$$Q_m = m_2 \delta_{col} + m_3 \tag{5.2}$$

where δ_{col} is the main rotor collective control and m_1, m_2 and m_3 are parameters.

Therefore, the main rotor forces and moments equations (2.141) - (2.146) transform to

$$X_m = -m_1 \delta_{col} a_1 \tag{5.3}$$

$$Y_m = m_1 \delta_{col} b_1 \tag{5.4}$$

$$Z_m = -m_1 \delta_{col} \tag{5.5}$$

$$L_m = K_\beta b_1 + m_1 \delta_{col} h_m b_1 \tag{5.6}$$

$$M_m = K_\beta a_1 + m_1 \delta_{col} h_m a_1 \tag{5.7}$$

$$N_m = m_2 \delta_{col} + m_3 \tag{5.8}$$

Tail Rotor Forces and Moments

In low advance ratio flight, the tail rotor thrust and torque can be approximated as

$$T_t = m_4 \delta_{ped} \tag{5.9}$$

$$Q_t = -m_5 \delta_{ped} - m_6 \tag{5.10}$$

where δ_{ped} is the tail rotor pedal control and m_4, m_5 and m_6 are parameters.

Therefore, the tail rotor forces and moments equations (2.160) - (2.163) transform to

$$Y_t = m_4\delta_{ped} \tag{5.11}$$

$$L_t = m_4\delta_{ped}h_t \tag{5.12}$$

$$M_t = m_5\delta_{ped} + m_6 \tag{5.13}$$

$$N_t = -m_4\delta_{ped}l_t \tag{5.14}$$

Horizontal Stabilizer Forces and Moments

Recall equations (2.164) - (2.166):

$$\begin{aligned} w_h &= w + l_h q - K_\lambda v_i \\ Z_h &= -\frac{1}{2}\rho S_h(C_h u^2 + |w_h|w_h) \\ M_h &= Z_h l_h \end{aligned}$$

In low advance ratio flight $K_\lambda = 0$. Z_h and M_h can be represented as function of u, w and q expressed as

$$Z_h = m_7u^2 + m_8w^2 + m_9q^2 + m_{10}wq \tag{5.15}$$

$$M_h = (m_7u^2 + m_8w^2 + m_9q^2 + m_{10}wq)l_h \tag{5.16}$$

Vertical Fin Forces and Moments

Recall equations (2.167) - (2.171):

$$
\begin{aligned}
v_{it} &= -\lambda_{0t}\Omega_t R_t \\
v_v &= v - l_t r - \epsilon_v v_{it} \\
Y_v &= -\frac{1}{2}\rho S_v (C_v u^2 + |v_v| v_v) \\
N_v &= -Y_v l_t \\
L_v &= Y_v h_t
\end{aligned}
$$

In low advance ratio flight, v_{it} can be approximated as

$$v_{it} = m_0 \delta_{ped} \tag{5.17}$$

Therefore, forces and moments can be represented as

$$
\begin{aligned}
Y_v = \quad & m_{11}u^2 + m_{12}v^2 + m_{13}r^2 + m_{14}\delta_{ped}^2 \\
& + m_{15}vr + m_{16}v\delta_{ped} + m_{17}r\delta_{ped} \qquad (5.18) \\
N_v = \quad & (m_{11}u^2 + m_{12}v^2 + m_{13}r^2 + m_{14}\delta_{ped}^2 \\
& + m_{15}vr + m_{16}v\delta_{ped} + m_{17}r\delta_{ped})l_t \qquad (5.19) \\
L_v = \quad & (m_{11}u^2 + m_{12}v^2 + m_{13}r^2 + m_{14}\delta_{ped}^2 \\
& + m_{15}vr + m_{16}v\delta_{ped} + m_{17}r\delta_{ped})h_t \qquad (5.20)
\end{aligned}
$$

Fuselage Forces and Moments

In low advance ratio flight, u, v and w are relatively small compared to the main rotor induced velocity v_i. Therefore, the fuselage forces and moments equations (2.172)

- (2.174) are simplified as

$$X_f = -\frac{1}{2}\rho S_{xf} u v_i \tag{5.21}$$

$$Y_f = -\frac{1}{2}\rho S_{yf} v v_i \tag{5.22}$$

$$Z_f = -\frac{1}{2}\rho S_{zf} v_i^2 \tag{5.23}$$

Since v_i is a function of δ_{col}, equations (5.21) - (5.23) transform to

$$X_f = m_{18} u \delta_{col} \tag{5.24}$$

$$Y_f = m_{19} v \delta_{col} \tag{5.25}$$

$$Z_f = m_{20} \delta_{col}^2 \tag{5.26}$$

Overall Forces and Moments

Given the forces and moments of each component, the overall forces and moments can be described as

$$\begin{aligned} X = & \quad X_m + X_f \\ = & \quad -m_1 \delta_{col} a_1 + m_{18} u \delta_{col} \end{aligned} \tag{5.27}$$

$$\begin{aligned} Y = & \quad Y_m + Y_t + Y_v + Y_f \\ = & \quad m_1 \delta_{col} b_1 + m_4 \delta_{ped} + m_{11} u^2 + m_{12} v^2 + m_{13} r^2 + m_{14} \delta_{ped}^2 \\ & + m_{15} v r + m_{16} v \delta_{ped} + m_{17} r \delta_{ped} + m_{19} v \delta_{col} \end{aligned} \tag{5.28}$$

$$\begin{aligned} Z = & \quad Z_m + Z_h + Z_f \\ = & \quad -m_1 \delta_{col} + m_7 u^2 + m_8 w^2 + m_9 q^2 + m_{10} w q + m_{20} \delta_{col}^2 \end{aligned} \tag{5.29}$$

$$
\begin{aligned}
L = \quad & L_m + L_t + L_v \\
= \quad & K_\beta b_1 + m_1 \delta_{col} h_m b_1 + m_4 \delta_{ped} h_t + (m_{11} u^2 + m_{12} v^2 + m_{13} r^2 + m_{14} \delta_{ped}^2 \\
& + m_{15} vr + m_{16} v \delta_{ped} + m_{17} r \delta_{ped}) h_t \qquad (5.30) \\
M = \quad & M_m + M_t + M_h \\
= \quad & K_\beta a_1 + m_1 \delta_{col} h_m a_1 + m_5 \delta_{ped} + m_6 \\
& + (m_7 u^2 + m_8 w^2 + m_9 q^2 + m_{10} wq) l_h \qquad (5.31) \\
N = \quad & N_m + N_t + N_v \\
= \quad & m_2 \delta_{col} + m_3 - m_4 \delta_{ped} l_t + (m_{11} u^2 + m_{12} v^2 + m_{13} r^2 + m_{14} \delta_{ped}^2 \\
& + m_{15} vr + m_{16} v \delta_{ped} + m_{17} r \delta_{ped}) l_t \qquad (5.32)
\end{aligned}
$$

5.3.2 Linear Parametrization Model

Substituting equations (5.27) - (5.32) into the equations of motion of the helicopter (2.32) and applying linear parametrization [44] yields

$$
\begin{bmatrix}
m(\dot{u} + wq - vr + g \sin\theta) \\
m(\dot{v} + ur - wp - g \cos\theta \sin\phi) \\
m(\dot{w} + vp - uq - g \cos\theta \cos\phi) \\
I_{xx}\dot{p} - (I_{yy} - I_{zz})qr - K_\beta b_1 \\
I_{yy}\dot{q} - (I_{zz} - I_{xx})rp - K_\beta a_1 \\
I_{zz}\dot{r} - (I_{xx} - I_{yy})pq \\
\dot{\phi} - p - q \sin\phi \tan\theta - r \cos\phi \tan\theta \\
\dot{\theta} - q \cos\phi + r \sin\phi \\
\dot{\psi} - q \sin\phi \sec\theta - r \cos\phi \sec\theta \\
\dot{a_1} + q + \frac{a_1}{\tau_e} - \frac{\delta_{lon}}{\tau_e} \\
\dot{b_1} + p + \frac{b_1}{\tau_e} - \frac{\delta_{lat}}{\tau_e}
\end{bmatrix}
= P
\begin{bmatrix}
m_1 \\ m_2 \\ m_3 \\ \vdots \\ m_{21}
\end{bmatrix}
\qquad (5.33)
$$

where

$P_{(11\times21)} = [P_{1(11\times11)} \quad P_{2(11\times10)}]$,

$$P_1 = \begin{bmatrix}
-a_1\delta_{col} & 0 & 0 & 0 & 0 & 0 & 0 & 0 & 0 & 0 & 0 \\
\delta_{col}b_1 & 0 & 0 & \delta_{ped} & 0 & 0 & 0 & 0 & 0 & 0 & u^2 \\
-\delta_{col} & 0 & 0 & 0 & 0 & 0 & u^2 & w^2 & q^2 & wq & 0 \\
h_m\delta_{col}b_1 & 0 & 0 & h_t\delta_{ped} & 0 & 0 & 0 & 0 & 0 & 0 & h_tu^2 \\
\delta_{col}h_ma_1 & 0 & 0 & 0 & \delta_{ped} & 1 & l_hu^2 & l_hw^2 & l_hq^2 & l_hwq & 0 \\
0 & \delta_{col} & 1 & -\delta_{ped}l_t & 0 & 0 & 0 & 0 & 0 & 0 & l_tu^2 \\
0 & 0 & 0 & 0 & 0 & 0 & 0 & 0 & 0 & 0 & 0 \\
0 & 0 & 0 & 0 & 0 & 0 & 0 & 0 & 0 & 0 & 0 \\
0 & 0 & 0 & 0 & 0 & 0 & 0 & 0 & 0 & 0 & 0 \\
0 & 0 & 0 & 0 & 0 & 0 & 0 & 0 & 0 & 0 & 0 \\
0 & 0 & 0 & 0 & 0 & 0 & 0 & 0 & 0 & 0 & 0
\end{bmatrix}$$

$$P_2 = \begin{bmatrix}
0 & 0 & 0 & 0 & 0 & 0 & 0 & 0 & u\delta_{col} & 0 \\
v^2 & r^2 & \delta_{ped}^2 & vr & v\delta_{ped} & r\delta_{ped} & 0 & v\delta_{col} & 0 & 0 \\
0 & 0 & 0 & 0 & 0 & 0 & 0 & 0 & \delta_{col}^2 & 0 \\
h_tv^2 & h_tr^2 & 0h_t\delta_{ped}^2 & h_tvr & h_tv\delta_{ped} & h_tr\delta_{ped} & 0 & 0 & 0 & 0 \\
0 & 0 & 0 & 0 & 0 & 0 & 0 & 0 & 0 & 0 \\
l_tv^2 & l_tr^2 & l_t\delta ped^2 & l_tvr & l_tv\delta_{ped} & l_tr\delta_{ped} & 0 & 0 & 0 & 0 \\
0 & 0 & 0 & 0 & 0 & 0 & 0 & 0 & 0 & 0 \\
0 & 0 & 0 & 0 & 0 & 0 & 0 & 0 & 0 & 0 \\
0 & 0 & 0 & 0 & 0 & 0 & 0 & 0 & 0 & 0 \\
0 & 0 & 0 & 0 & 0 & 0 & 0 & 0 & 0 & u\delta col \\
0 & 0 & 0 & 0 & 0 & 0 & 0 & 0 & 0 & -v\delta col
\end{bmatrix}$$

5.3.3 Filtering Technique

The model (5.33) cannot be directly used for estimation because of the presence of the unmeasurable accelerations $\dot{u}$, $\dot{v}$, $\dot{w}$, $\dot{p}$, $\dot{q}$ and $\dot{r}$. A filtering technique can be used to solve the problem [44]. To avoid the acceleration in this relation, let us filter both sides of the equation by $\frac{1}{s+\lambda_f}$ (where s is the Laplace operator and λ_f is a known positive constant). Rearranging, this leads to the form

$$\begin{bmatrix} m(u - \lambda_f u_f + w_f q - v_f r + \frac{g\sin\theta}{s+\lambda_f}) \\ m(v - \lambda_f v + u_f r - w_f p - \frac{g\cos\theta\sin\phi}{s+\lambda_f}) \\ m(w - \lambda_f w + v_f p - u_f q - \frac{g\cos\theta\cos\phi}{s+\lambda_f}) \\ I_{xx}(p - \lambda_f p) - (I_{yy} - I_{zz})q_f r - K_\beta b_{1f} \\ I_{yy}(q - \lambda_f q) - (I_{zz} - I_{xx})r_f p - K_\beta a_{1f} \\ I_{zz}(r - \lambda_f r) - (I_{xx} - I_{yy})p_f q \\ \phi - \lambda_f\phi - p_f - q_f\sin\phi\tan\theta - r_f\cos\phi\tan\theta \\ \theta - \lambda_f\theta - q_f\cos\phi + r_f\sin\phi \\ \psi - \lambda_f\psi - q_f\sin\phi\sec\theta - r_f\cos\phi\sec\theta \\ a_1 - \lambda_f a_1 + q_f + \frac{a_{1f}}{\tau_e} - \frac{\delta_{lonf}}{\tau_e} \\ b_1 - \lambda_f b_1 + p_f + \frac{b_{1f}}{\tau_e} - \frac{\delta_{latf}}{\tau_e} \end{bmatrix} = P_f \begin{bmatrix} m_1 \\ m_2 \\ m_3 \\ \vdots \\ m_{20} \end{bmatrix} \tag{5.34}$$

where $()_f$ denotes $\frac{()}{s+\lambda_f}$. Matrix P_f is obtained by filtering each entry of the matrix P by $\frac{1}{s+\lambda_f}$.

5.3.4 The Gradient Estimator

In this section a prediction-error-based estimation method called the gradient estimation [44] is introduced. The basic idea in gradient estimation is that the parameter should be updated such that the prediction error is reduced. The parameter vector in (5.34) is unknown and is estimated to be $\hat{a}(t)$ at time t. One can predict the value

of the output $y(t)$ based on the parameter estimate and the model (5.34) as

$$\hat{y}(t) = W(t)\hat{a}(t) \tag{5.35}$$

where $\hat{y}(t)$ is called the predicted output at time t. The difference between the predicted output and the measured output $y(t)$ is called the prediction error, i.e.

$$e_1(t) = \hat{y}(t) - y(t) \tag{5.36}$$

The gradient estimator is written as

$$\dot{\hat{a}} = -p_o W^T e_1 \tag{5.37}$$

Substituting (5.35) and (5.36) into (5.37), the estimator is represented as

$$\dot{\hat{a}} = -p_o W^T W \hat{a} + p_o W^T y \tag{5.38}$$

where in our case $W = P_f$, $a = [m_1 \quad m_2 \cdots m_{21}]^T$ and

$$y = \begin{bmatrix} m(u - \lambda_f u_f + w_f q - v_f r + \frac{g \sin\theta}{s+\lambda_f}) \\ m(v - \lambda_f v + u_f r - w_f p - \frac{g \cos\theta \sin\phi}{s+\lambda_f}) \\ m(w - \lambda_f w + v_f p - u_f q - \frac{g \cos\theta \cos\phi}{s+\lambda_f}) \\ I_{xx}(p - \lambda_f p) - (I_{yy} - I_{zz}) q_f r - K_\beta b_{1f} \\ I_{yy}(q - \lambda_f q) - (I_{zz} - I_{xx}) r_f p - K_\beta a_{1f} \\ I_{zz}(r - \lambda_f r) - (I_{xx} - I_{yy}) p_f q \\ \phi - \lambda_f \phi - p_f - q_f \sin\phi \tan\theta - r_f \cos\phi \tan\theta \\ \theta - \lambda_f \theta - q_f \cos\phi + r_f \sin\phi \\ \psi - \lambda_f \psi - q_f \sin\phi \sec\theta - r_f \cos\phi \sec\theta \\ a_1 - \lambda_f a_1 + q_f + \frac{a_{1f}}{\tau_e} - \frac{\delta_{lonf}}{\tau_e} \\ b_1 - \lambda_f b_1 + p_f + \frac{b_{1f}}{\tau_e} - \frac{\delta_{latf}}{\tau_e} \end{bmatrix}$$

Therefore, if we are given the continuous measurements of $y(t)$ and $W(t)$, i.e. u, v, w, p, q, r, a_1, b_1, δ_{col} and δ_{ped}, we can solve equation (5.38) for the unknown parameter vector a.

References

[1] E. F. S. Boyd, L. El Ghaoui, and V. Balakrishnan. *Linear Matrix Inequalities in System and Control Theory (Studies in Applied Mathematics).* Philadelphia: SIAM, 1994.

[2] A. R. S. Bramwell. *Bramwell's Helicopter Dynamics.* AIAA, 2001.

[3] E. Frazzoli. *Robust Hybrid Control for Autonomous Vehicle Motion Planning.* PhD thesis, Department of Aeronautics and Astronautics, Massachusetts Institute of Technology, Cambridge, MA, June 2001.

[4] E. Frazzoli, M. A. Dahleh, and E. Feron. Real-time motion planning for agile autonomous vehicles. *AIAA Journal of Guidance, Control, and Dynamics*, 25(1):116–129, 2002.

[5] Dario Fusato, Giorgio Guglieri, and Roberto Celi. Flight dynamics of an articulated rotor helicopter with an external slung load. Presented at the American Helicopter Society 55th Annual Forum, May 1999.

[6] V. Gavrilets, B. Mettler, and E. Feron. Nonlinear model for a small-size aerobatic helicopter. In *Proceedings of the AIAA Conference on Guidance, Navigation and Control*, Montreal, Canada, August 2001.

[7] PENOPT GbR. Penbmi manual, 2005. Available at http://www.penopt.com/.

[8] A. González, R. Mahtani, M. Béjar, and A. Ollero. Control and stability analysis of an autonomous helicopter. Technical report, Universidad de Sevilla, Spain, 2004.

[9] R.K. Heffley, Jewell, J.M. Lehmam, and R.A. Von Winkle. A compilation and analysis of helicopter handling qualities data; volume i: Data compilation. NASA CR 3144, August 1979.

[10] S.J. Ingle and R. Celi. Effects of higher order dynamics on helicopter flight control law design. *Journal of American Helicopter Society*, 39(1):50–61, July 1994.

[11] M. Johanson. *Piecewise Linear Control Systems*. Springer Verlag, 2003.

[12] E. N. Johnson, A. A. Proctor, J. Ha, and A. R. Tannenbaum. Development and test of highly autonomous unmanned aerial vehicles. *AIAA Journal of Aerospace Computing, Information, and Communication*, 1(12):485–501, December 2004.

[13] Eric N. Johnson and Paul A. DeBitetto. Modeling and simulation for small autonomous helicopter developement. In *Proceedings of the AIAA Modeling and Simulation Technologies Conference*, 1997.

[14] H. K. Khalil. *Nonlinear systems*. Prentice Hall, third edition, 2002.

[15] H. Jin Kim, David H. Shim, and Shankar Sastry. A flight control system for aerial robots: Algorithms and experiments. Technical report, EECS Department, University of California, Berkley, Berkley, CA, USA, April 2003.

[16] T.J. Koo and S. Sastry. Output tracking control design of a helicopter model based on approximate linearization. In *Proceedings of IEEE Conference on Decision and Control*, volume 4, pages 3635–3640, December 1998.

[17] J. M. Krodkiewski. Stabilization of motion of helicopter rotor blades using delayed feedback - modelling, computer simulation and experimental verification. *Journal of Sound and Vibration*, 24(4):591–610, 2000.

[18] Advanced Optimization Laboratory. Sedumi 1.1, 2004. Available at http://sedumi.mcmaster.ca/.

[19] Automatic Control Laboratory. Yalmip, 2005. Available at http://control.ee.ethz.ch/ joloef/yalmip.php.

[20] M. LaCivita, W. Messner, and T. Kanade. Modeling of small-scale helicopters with integrated first-principles and integrated system identification techniques. Presented at 58th Forum of American Helicopter Society, June 2002.

[21] J. Gordon Leishman. *Principles of Helicopter Aerodynamics.* Cambridge University Press, New York, 2000.

[22] L. Ljung. *System Identification: Theory for the User.* Prentice Hall, Saddle River, N.J., 1999.

[23] B. Mettler. *Identification, Modeling and Characteristics of Miniature Rotorcraft.* Kluver Academic Publishers, Boston, MA, 2002.

[24] B. Mettler. System identification modeling of a small-scale unmanned rotorcraft for control design. *Journal of the American Helicopter Society,* 47(1):50–63, January 2002.

[25] B. Mettler, T. Kanade, and M. Tishler. System identification modeling of a model-scale helicopter. Technical report, Robotics Institute, Carnegie Mellon University, Cambrigde USA, January 2000.

[26] B. Mettler, Mark B. Tischler, and Takeo Kanade. System identification of small-size unmanned helicopter dynamics. Presented at the American Helicopter Society 55th Forum, Montreal, Quebec, Canada, May 1999.

[27] Huba Mikuláš, Karas Miloš, and Veličko Viktor. The helicopter rack control. Technical report, Slovak University of Technology, Bratislava, 2000.

[28] Ben Motazed and David Vos. Aerodynamics and flight control design for hovering micro air vehicles. In *Proceedings of the American Control Conference,* volume 2, pages 681–683, Philadelphia, Pennsylvania, June 1998.

[29] Christian Munzinger. Development of a real-time flight simulator for an experimental model helicopter. Master's thesis, Georgia Institute of Technology, Atlanta, GA, 1998.

[30] Gareth D. Padfield. *Helicopter Flight Dynamics: The Theory and Application of Flying Qualities and Simulation Modeling.* AIAA education series, 1996.

[31] Mario G. Perhinschi. Controller design for autonomous helicopter model using a genetic algorithm. Presented at the American Helicopter Society 53rd Annual Forum, April 1997.

[32] Raymond W. Prouty. *Helicopter Performance, Stability, and Control.* PWS Publishers, 1986.

[33] Sven Rebeschieß and Marc Roloff. Position control by feedback linearization for a simplified helicopter model. In *Proceedings of the 1999 IEEE International Conference on Control Applications*, volume 1, pages 143–145, Hawaii, USA, August 1999.

[34] Luis Rodrigues. *Dynamic Output Feedback Controller Synthesis For Piecewise-Affine Systems.* PhD thesis, Stanford University, 2002.

[35] Luis Rodrigues, Arash Hassibi, and Jonathan P. How. Output feedback controller synthesis for piecewise-affine systems with multiple equilibria. In *Proceedings of the American Control Conference*, pages 1784–1789, Chicago, Illinois, USA, June 2000.

[36] Luis Rodrigues and Jonathan P. How. Automated control design for a piecewise-affine approximation of a class of nonlinear systems. In *Proceedings of the American Control Conference*, pages 3189–3194, Arlington, Virginia, USA, June 2001.

[37] Luis Rodrigues and Jonathan P. How. Observer-based control of piecewise-affine systems. *International Journal of Control*, 76(5):459–477, 2003.

[38] Luis Rodrigues and Jonathan P. How. Synthesis of piecewise-affine controllers for stabilization of nonlinear systems. In *42nd IEEE Conference on Decision and Control*, pages 2071–2076, Maui, Hawaii, December 2003.

[39] J. M. Rolfe and K. J. Staples. *Flight Simulation.* Cambridge University Press, UK, 1986.

[40] Behzad Samadi and Luis Rodrigues. Piecewise-affine controller synthesis based on a local linear controller: Toolbox for MATLAB using the PENBMI solver. Technical report, Concordia University, 2005.

[41] S.T. Shaw and N. Qin. Study of the aerodynamics of in-plane motion. Technical report, Cranfield College of Aeronautics, Cranfield, UK, 1999.

[42] H. Shim, T.J. Koo, F.Hoffmann, and S. Sastry. A comprehensive study of control design for an autonomous helicopter. In *Proceedings of IEEE Conference on Decision and Control*, volume 4, pages 3653–3658, Florida, December 1998.

[43] Erik Skarman. A helicopter model. Technical report, Linkoing electronic articles in computer and information science, Cambrigde USA, 1999.

[44] Jean-Jacques E. Slotine and Weiping Li. *Applied Nonlinear Control.* Prentice Hall, 1991.

[45] Robert F. Stengel. *Flight Dynamics.* Princeton University Press, Princeton, N.J., 2004.

[46] W. Z. Stepniewski and C. N. Keys. *Rotary-Wing Aerodynamics.* Dover Publications, Inc., New York, 1984.

[47] M. Sugeno, I. Hirano, S. Nakamura, and S. Kotsu. Development of an intelligent unmanned helicopter. In *IEEE International Conference on Fuzzy Systems*, 1995.

[48] M. Tischler. *Advances in Aircraft Flight Control.* Taylor and Francis, Cornwall, England, 1996.

[49] John Watkinson. *The Art of the Helicopter.* Elsevier Butterworth-Heinemann, 2004.